Heliyon 10 (2024) e39954

Contents lists available at ScienceDirect

Heliyon

journal homepage: www.cell.com/heliyon

Research article

Experimental and numerical study of dissimilar fiber laser welding of martensitic AISI 1060 carbon steel with different configuration with austenitic 304 and ferritic 420 stainless steel

Akbar Zarei [a], Mohammad Akbari [a,b,*], Ali Abdollahi [c,d], Hamid Soleimanimehr [c,d]

[a] Department of Mechanical Engineering, Najafabad Branch, Islamic Azad University, Najafabad, Iran
[b] Aerospace and Energy Conversion Research Center, Najafabad Branch, Islamic Azad University, Najafabad, Iran
[c] Department of Mechanics, Electrical Power and Computer, Science and Research Branch, Islamic Azad University, Tehran, Iran
[d] Modern Automotive Research Center, Science and Research Branch, Islamic Azad University, Tehran, Iran

ARTICLE INFO

Keywords:
Dissimilar laser welding
Temperature field
AISI 1060
420 stainless steel
304 stainless steel
Microstructure

ABSTRACT

Welding with fiber laser for two distinct stainless steel types was performed to join with the martensitic carbon steel (AISI 1060) in order to assess the effect of laser welding operating parameters for two dissimilar materials on the weld characterization thorough experimental design method and numerical investigation. A full central composite design (CCD) matrix in accordance with the response surface methodology (RSM) was developed to represent the responses variations by equations including quadratic and nonlinear interaction terms. Different laser welding parameters were taken into account, such as laser power, linear speed of welding, focal distance of the beam, and beam deviation. The responses considered were the temperature field next to the melt pool border line, the maximum penetration depth of the fusion zone and the ultimate tensile strength of the dissimilar weld joint. Additionally, the variation of the microstructure fusion zone and adjacent areas and failure mechanism of the weld joint were evaluated. The experimental results indicate that the temperature field measured at the vicinity of the melt pool fusion line with both 304 and 420 stainless steel which primarily influenced by the incident power of the laser and linear velocity of beam, respectively. Additionally, the numerical simulation results are in good agreement with temperature experimental results at vicinity of fusion line where the temperature measured, experimentally. Apart from this, at the center of the fusion zone, the temperature clearly predicts via numerical simulation results which is not possible to assess experimentally. A clear comparison between the temperature distribution with different joint configuration illustrates that distinct relation between the temperature variation rate and different thermal conductivity coefficient of AISI 1060 with different AISI 304 and 420 joint configuration resulted different temperature distribution. The weld joint microstructure for 420 stainless steel–AISI 1060 steel joint at fusion boundary zone consists of columnar dendrites and skeletal columnar ferrite. At the center of fusion zone, a cellular-type structure is seen. For 304 stainless steel joint, the fusion zone has composed of a remarkable part of skeletal delta-ferrite and dendritic microstructure at austenite matrix microstructure. The fracture section of 304

* Corresponding author. Department of Mechanical Engineering, Najafabad Branch, Islamic Azad University, Najafabad, Iran.
E-mail address: m.akbari.g80@gmail.com (M. Akbari).

https://doi.org/10.1016/j.heliyon.2024.e39954
Received 2 July 2024; Received in revised form 26 October 2024; Accepted 28 October 2024
Available online 29 October 2024

steel has a ductile fracture and the depth of fracture dimples and cavities toward 304 stainless steel are higher than AISI 1060 steel.

Nomenclature		Unit
h	*heat transfer coefficient*	$W/m^2\,K$
$\overline{u}$	*mean velocity*	m/s
P	*pressure*	N/m^2
$X.Y.Z$	*Cartesian coordinates*	
C	*specific heat capacity*	$J/kg\,K$
T	*Temperature*	K
t	time s	
H	*enthalpy J*	
k	*thermal conductivity*	$W/m\,K$
u, v, w	*velocities components in X,Y and Z directions*	m/s
q	*heat flux*	W/m^2
f_c	distribution coefficient	
K_0	*constant of the mushy zone*	
S_V	*energy equation source term*	
f	POW Liquid fraction Laser Power W	
SP	mm/min	
Dev	Deviation mm	
FD	Focal Distance mm	
Greek symbols	mm	
ρ	*density*	kg/m^3
μ	*dynamic viscosity*	*Pa s*
ϑ	*kinematics viscosity*	m^2/s
β	*thermal expansion coefficient*	$1/K$
σ	*Boltzmann constant*	

1. Introduction

The advancement of laser welding technologies has significantly transformed the landscape of material joining, particularly when addressing dissimilar materials. Fiber laser welding, renowned for its precision and efficiency, is increasingly applied to join different types of metals, such as carbon steels and stainless steels [1–3]. Recent studies have highlighted the complexity of laser welding dissimilar metals, emphasizing the need for a detailed understanding of the temperature distribution, weld microstructure, and mechanical properties of the joints [4,5]. The development of advanced numerical models and experimental techniques has facilitated a deeper exploration into these aspects [6,7]. For instance, large eddy simulation studies have provided insights into the flow characteristics during welding processes, while recent advances in laser technology have enhanced our ability to control and predict welding outcomes [8–10]. Welding of dissimilar materials joint including austenitic and ferritic stainless steel with different types of low to moderate carbon steels configuration by different lasers types has been investigated at previous studies. Due to the wide application in automotive, petrochemical, military industries, the construction of steel tanks and high-load sections, using the laser welding method of these steels compared to other methods can provide advantages such as controlling the welding parameters to achieve a connection with desirable quality properties, high productivity as well as suitable appearance [11,12]. Dissimilar laser welding of carbon is known as a more challenging method due to creation of brittle and susceptible to hydrogen-induced cold cracking induced by high carbon content as well as high cooling rate of laser welding [13]. Therefore, dissimilar welding of carbon steel by other materials can be a promising alternate as utilized by karimi et al. [14]. Their investigation focused on the laser process parameters impact on analyzing the microstructure, temperature distribution, and the joint mechanical characteristics between A516 steel and duplex stainless steel. They reported effective alloy composition at fusion zone and highlighted higher fracture ductility of the dissimilar joints welded at higher laser power levels [14].

In dissimilar laser welding, mutual solubility and homogeneous dissimilar weld bead joints with minimal variations in mechanical properties are important issues that highlighted in some dissimilar laser welding researches [15–20].

Zhang et al. [8] investigated laser keyhole welding between duplex stainless steel 2205 and low carbon steel (A516) via computational modeling and experimental investigation. A multiphysics model was developed to achieve an accurate simulation of the temperature and velocity fields. The numerical simulation results were in agreement with temperature filed and melt flow experimental results. The predicted melt pool geometry from the simulation results (melt flow and temperature field) was in good agreement with the experimental results. Furthermore, the temperature distribution from simulation results effectively predict the microstructural changes of the melt pool region according to the melting, solidification and temperature gradient at the melt pool and adjacent HAZ regions. Poornima et al. [21] investigated experimental and numerical simulation of dissimilar laser welding of UNS S32304 and SS304L technique to enhance the ductility of the structure under critical conditions. A response surface Methodolog was utilized to statistically analyze and optimize the outcomes. By utilizing ANSYS software and considering different clearance gaps between base metals, variation of the beam diameter, Heat Affected Zone Temperature and force the optimized results including Bead Width

Clearance (BWC) of 1.00687 mm, beam diameter of 1.00469 mm, HAZT of 1500.41 °C, and force of 6482.06 kN. Unni el al [22]. proposed a way to select appropriate heat source model for predicting the temperature distribution fluid flow dynamic behavior during keyhole Laser welding of Type 316 LN stainless steel. By application of different heat source models including volumetric heat sources namely, 3D conical, a coalition of 3D conical and cylindrical heat source, 3D volumetric Gaussian and Rotary Gaussian, finally the conical-cylindrical combined (CCC) model exhibited good agreement with actual weld bead dimensions and thermal data extracted from the experiments. Ai et al. [23] developed 3D numerical calculation model to predict the weld bead formation process in laser welding of dissimilar materials. The temperature distribution and melted material flow based on thermophysical properties for the numerical simulation results were gained. different thermophysical properties, the temperature field, and the flow field are asymmetric in the laser welding of dissimilar materials. The influence of asymmetrical flow field on both sides of the dissimilar melt pool is known as the critical factor for the generation of asymmetric behaviors in the dissimilar material fiber laser welding. Cui et al. [24] examined the utilization of the butt fiber laser welding technique on AISI 304 austenitic stainless steel with varying thicknesses of 3 and 6 mm. The Argon shielding gas was employed during the welding process. Their study was focused on assessing the quality of the welded joint in terms of its appearance, microstructure, elemental composition, and hardness. Their results showed that utilizing a laser power of 2 KW along with a linear welding velocity of 20 mm/s, resulted in the creation of a defect free joint with complete penetration depth. Different microstructures were usually formed in various regions of the fusion zone including micro-columnar and moderate-axis crystals were present at the edge and center of the weld. Furthermore, the improved strength of the welded connection in the stainless steel layers was primarily due to the more refined microstructure. Meng et al. [25] evaluated the application of butt welding with pulsed laser on stainless steel dissimilar plates of AISI 321 and ferritic AISI 405.

They analyzed the impact of pulse laser settings on the formation of weld beads, mechanical characteristics and weld joints microstructure. At frequency range of 400–600 Hz and a duty cycle at range of 30–50 % dissimilar joints with superior quality were created. The mixed structure of austenite and ferrite caused the microhardness to be significantly higher than that base metals.

Yan et al. [26] explored laser welding techniques on Inconel 625 and stainless steel 304 dissimilar joint. The research focused on monitoring temperature changes through modifications in laser parameters such as incident beam power, linear speed of welding and nozzle distance. Notably, adjustments in power level had more pronounced effect on the temperature variations at the region near the melt pool of Inconel 625. The lower temperature augmentation in stainless steel 304 was attributed to the portion of the laser beam absorption by the melted material evaporation. Geng et al. [27] evaluated the pulsed Nd: YAG AISI 304 austenitic and 420 ferritic stainless steel. The study involved an analysis of microstructure, mechanical characterizations of the welded joints and distribution of temperature from the fusion zone to the base metals. Furthermore, the study explored the influence of different pulsed laser characterization including duration of pulse, pulse frequency, and total current instead of the laser average power. The disparity in thermal conductivities between two different materials led to the higher level of the temperature within the dissimilar weld zone for the austenitic material attributed to the greater heat concentration. Within the fusion zone central region, the microstructure consisted of predominantly austenite and coarse ferrite grains, which accounted for approximately more than 70 % of the molten pool volume. Moving into the heat affected region, the microstructure exhibited coarse grains of ferrite in proximity to the ferritic base metal, while the austenite side showed a combination of austenite grains with embedded ferrite strands. The joint tensile strength was significantly reduced by approximately 30 % as the welding speed was increased. Moreover, when the temperature at the region near the melt pool remarkably reduced from 250 °C to 130 °C during welding, it resulted in an enhanced possibility of porosity formation [27].

Wenyong et al. [28] carried out research on the microstructural properties, variation of mechanical characterization and corrosion resistance of dissimilar joints between carbon steel and ferritic stainless steel. The results imply that the microstructure of this heterogeneous weld is predominantly martensitic. Augmentation of the welding speed led to the smaller of the heat-affected zone (HAZ) width for carbon steel and an increase in hardness adjacent to the ferritic side. Although the joints welded at varying speeds exhibited comparable ultimate tensile strength. at slower speeds, the joints displayed a superior level of elongation compared to the welded joints at high-speed. Torkamany et al. [29] conducted a study to examine the welding mode impact on the laser spot welding characterization including microstructure and mechanical characterizations of dissimilar low carbon steel and austenitic stainless steels. The study indicated that when the mean laser power rises, the welding mode undergoes a transition from conduction mode to keyhole. The transition to keyhole mode results in a significant increase in fusion zone dimension in the low carbon steel sheet. This is mainly related to the increasing absorption of incident laser beam energy due to the formation of keyholes. Moreover, it was demonstrated that the fusion zone dimensions have a remarkable effect on determining the mechanical strength of non-homogeneous laser welds between austenitic and ferritic dissimilar joints. Anawa and Olabi employed design of experiments techniques, specifically Taguchi and RSM to statistically analyze the weld geometry variation according to the laser welding operating parameters. Their aim was optimization the parameters of laser welding process for various materials such as stainless steel, steel, and carbon steels, focusing on the weld geometry [30–32].

Although numerous studies have been conducted to evidently identify the laser welding conditions impact on microstructure, mechanical properties, alloy composition and weld geometry of different stainless steels and carbon steel materials through various analysis methods, there is no comprehensive study on fiber laser welding for dissimilar stainless steels and AISI 1060 carbon steel. The high carbon content of AISI 1060 steel, hydrogen-induced cracking and solidification cracking significantly reduced the weld ability of this material. Additionally, high cooling rate during laser welding could make new challenge on welding of this material.

Hence, this study aims to conduct an experimental investigation using experimental design techniques to analyze the impact of laser welding process variables on the characterization of dissimilar weld joints between low weldability AISI 1060 carbon steel and two austenitic and ferritic stainless steels.

The AISI 1060 steel known as the carbon steel and laser welding of such materials has difficulties such as cracking just after welding. The high temperature gradient and fast cooling rate can worsen the welding condition of this material. On the other hand,

higher thermal conductivity of AISI 1060 can induce higher cooling rate at fusion zone. Therefore, fast heating and sever cooling rate notably increase the possibility formation of martensitic microstructure and solidification cracking. The demands for producing dissimilar joint by laser welding were classified as following. The first one is producing the joint with higher corrosion resistance which uses AISI 304 austenitic stainless steel. Furthermore, the austenitic microstructure of the weld and lower thermal conductivity have clear impact on the weld microstructure, weld defects and even mechanical properties. On the other hand, to achieve the dissimilar joint with higher mechanical properties, 420 stainless steel and AISI 1060 steel were utilized. For this joint configuration, although higher strength of the base metals existed, the higher thermal conductivity has significant influence on formation of martensitic microstructure at the fusion zone of dissimilar joint. Therefore, making a clear comparison between the joints mechanical properties (tensile strength), weld defects and microstructural properties were the main aims of this study. As a result, dissimilar joints microstructure, mechanical properties, temperature field during welding and weld defects according to utilizing different combination of chemical and physical properties of the weld joints configuration were clearly compared.

2. Dissimilar laser welding experimental configuration

The parts made of AISI 304 austenitic and AISI 420 ferritic steel stainless in accordance with AISI 1060 carbon steel were used for welding experiments. The material thickness was 1.5 mm and the welding samples dimensions were 20 × 50 mm for welding experiments. The materials chemical composition and physical properties are observed in Table 1.

For welding, a fiber laser with nominal ultimate power of 1000 W with continuous wave along with Raytools BW240 welding head with QBH connector were implemented for welding experiments. An extra side below nozzle for protection of melt pool by argon gas was utilized. A CNC table with 3 interpolated axis equipped with step motor and NC studio cam software were used for laser beam movement and accurate positioning the irradiated beam. For temperature measurement, two thermocouples with Type-K and diameter of 1 mm inserted at the grooves provided by electro discharge machining. Fig. 1 presents an observed representation of the experimental setup for laser welding, both in schematic and real view. The temperature data was obtained by converting the analog signal from thermocouples using the USB 4718 DAQ module and LABVIEW software. The samples were under preparation and polishing before being etched according to ASTM E3 standard for metallographic analysis. For microstructural analysis, an optical microscope Olympus model BX53M was utilized to provide images from the fusion zone weld and base metals. The mechanical strength of the weld joint evaluated by tensile test of welded joints performed using AL7000-MT universal tensile testing machine. Tensile tests samples preparation was done according to the standard of ASTM E8.

3. Experimental design

To estimate the impact of varying laser welding process parameters on AISI 1060 steel in combination with different types of stainless steels including austenitic and ferritic, the temperature at the region in the vicinity of the melt pool fusion line and base metals (AISI 1060 steel with austenitic steel and AISI 1060 steel with ferritic steel) was measured. Additionally, geometry variation of the molten pool (depth and width) and welded joint tensile strength were selected as the responses. In order to comprehensively evaluate the laser parameter's impact on the response levels, CCD method of experimental design was utilized. The input variables were chosen as the laser power parameters, changes in laser beam focal point position in relation to the top surface of the workpiece, the linear speed of the laser beam, and the laser beam deviation from the weld bead joint center line. By conducting a number of preliminary experiments, the initial limits of the parameters were evaluated. The main experiments process parameters levels were determined to evaluate and select the parameters levels of the main experimental design matrix. Table 2 shows the initial suggested conditions of the parameters for laser welding involves joining AISI 1060 steel with ferritic 420 and austenitic 304 stainless steel. The laser power and welding speed considered as two basic parameters that can play an important role in weld ability with suitable penetration for welding of AISI 1060 steel with two dissimilar stainless steels. The dissimilar laser welding process parameters levels is illustrated in Table 3. The chosen levels of output beam power and moving speed of laser beam are carried out in a wider range of changes than other parameters. In Table 4, the total number of 29 tests includes 5 points for the center of the cube matrix, 8 axial points and 16 cube surfaces points. This set of tests was done separately for each austenitic and ferritic steel.

4. Numerical simulation

A computer model based on computational fluid dynamics (CFD) was developed to investigate keyhole laser welding. The model is

Table 1
The materials chemical composition and physical characterization [33].

Material	C	Mn	Si	P	S	Cr	Ni	Fe
AISI 420	0.15	1	1	0.040	0.03	14.0		Bal
AISI 304	0.08	2	1	0.04	0.03	18	8	Bal
AISI 1060	0.6	0.55		0.04	0.04	–		Bal
Physical properties	**Thermal conductivity (W/m.K)**		**Melting point (°C)**		**Yield Tensile Strength (MPa)**		**Ultimate Tensile Strength (MPa)**	
AISI 420	16.2		1450		210		510	
AISI 304	24.9		1723		310		590	
AISI 1060	49.8		1510		340–700		670–860	

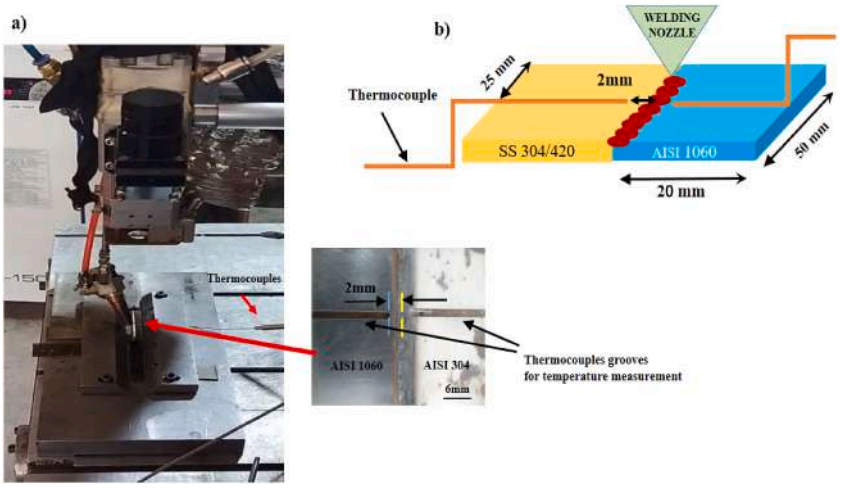

Fig. 1. The dissimilar laser welding setup of experiments for a) actual view, b) schematic view.

Table 2
Elementary dissimilar laser welding experiments.

Exp. No	Laser power (W)	Welding speed (mm/min)	Focal distance (mm)	Beam deviation (mm)
1	400	200	0	0.5
2	200	400	2	0.0
3	150	300	0	0.5
4	400	250	5	−0.5
5	200	300	1	−0.5
6	500	350	3	0.0

Table 3
The parameters levels.

parameter	Laser power (W)	Welding speed (mm/min)	Focal distance (mm)	Beam deviation (mm)
level	250–450	150–350	(-2)- (+6)	(-1)-(+1)

three-dimensional and time-dependent, using the finite volume method for calculations. the solidification/melting models was used to simulate the interactions between solid, and liquid phases. The model accounted for various welding phenomena such as temperature-dependent material properties, heat losses via convection and radiation, and phase changes of the material. The distribution of thermal flux through the Gaussian surface and the thermal source were employed as a means to model the energy absorbed from the laser beam irradiation. This is due to the fact that in the keyhole welding process, the plasma generated at the surface of the workpiece absorbs a portion of the energy. The following equations elucidate the surface and volumetric thermal fluxes. The surface heat flux was considered the boundary condition, and the volumetric heat flux was considered the source term in the energy equation [34–36]. Fig. 2 depicts a schematic representation of the amalgamation of thermal models.

$$q_s(x,y) = \frac{3f_1\eta p}{\pi r_s^2}\ exp\left(-3\frac{(x^2+y^2)}{r_s^2}\right) \tag{1}$$

$$q_v(x,y,z) = \frac{6f_2\eta p}{\pi r_v^2 d}\ exp\left(-3\frac{(x^2+y^2)}{r_v^2}\right)\left(\frac{mz+r_v}{md+2r_v}\right) \tag{2}$$

Where q_s represents the thermal flux emanating from the surface, q_v denotes the thermal source, p symbolizes the potency of the laser, f are the coefficients that govern the distribution of power, d indicates the cylindrical configuration of the thermal source, r characterizes radii of the surface thermal flux and the cylindrical heat source, η represents the coefficient of absorption, and m is the damping factor of the heat source, which is estimated through diverse simulations.

4.1. Governing equations

Keyhole laser welding involves the utilization of highly concentrated beam intensity for material processing applications. This technique facilitates the generation of metallic vapor in proximity to the molten metal, resulting in the displacement of a portion of the

Table 4
CCD experimental design main matrix.

EXP. No.	Laser power (W)	Welding speed (mm/min)	Focal distance (mm)	Beam deviation (mm)	Depth (mm)	Width (mm)	Temp (AISI 304) (°C)	Temp AISI (1060/304) (°C)	Temp (AISI 420) (°C)	Temp AISI (1060/420 (°C)	Tensile strength AISI (1060/304) (MPa)	Tensile strength AISI (1060/420) (MPa)
1	350	250	2	0	1.12	1.68	204	185	223	177	385	445
2	400	200	0	−0.5	1.44	1.95	274	288	302	251	557	612
3	350	250	6	0	0.94	1.75	208	144	226	154	345	435
4	450	250	4	0	1.50	2.1	312	321	338	305	518	595
5	350	250	2	0	1.10	1.44	194	220	207	198	385	458
6	350	250	2	0	1.12	1.52	221	250	261	215	412	445
7	300	300	0	−0.5	0.82	1.32	104	176	117	171	310	338
8	400	300	0	−0.5	1.23	1.74	194	260	218	243	448	547
9	300	300	0	0.5	0.78	1.39	158	146	176	138	305	362
10	350	250	2	1	0.98	1.48	197	197	216	188	386	436
11	400	300	4	0.5	1.37	1.78	212	210	229	192	384	453
12	300	200	0	0.5	0.87	1.52	181	186	188	174	368	398
13	250	250	2	0	0.74	1.28	107	157	118	152	278	312
14	350	250	−2	0	0.98	1.72	182	268	206	242	421	473
15	400	200	0	0.5	1.38	1.94	283	295	304	268	510	558
16	300	200	0	−0.5	1.28	1.65	153	193	178	173	392	428
17	300	300	4	−0.5	0.95	1.57	102	155	113	149	325	368
18	400	200	4	0.5	1.38	1.85	304	304	316	294	476	534
19	350	250	2	−1	1.18	1.62	143	188	166	166	418	539
20	300	200	4	0.5	0.92	1.79	158	149	187	141	382	426
21	400	300	4	−0.5	1.12	1.73	206	214	218	206	446	562
22	400	200	4	−0.5	1.32	1.92	248	248	288	226	534	632
23	350	250	2	0	1.23	1.66	241	210	271	201	398	453
24	350	350	2	0	0.96	1.38	154	168	177	153	316	385
25	300	200	4	−0.5	1.26	1.51	164	172	183	162	346	437
26	400	300	0	0.5	1.38	1.65	278	213	293	193	438	516
27	350	250	2	0	1.15	1.55	239	238	269	188	436	477
28	300	300	4	0.5	0.75	1.37	192	123	208	121	296	343
29	350	150	2	0	1.32	1.83	278	227	283	193	449	512
30	350	250	2	1	0.34	1.55	185	184	785	197	348	432

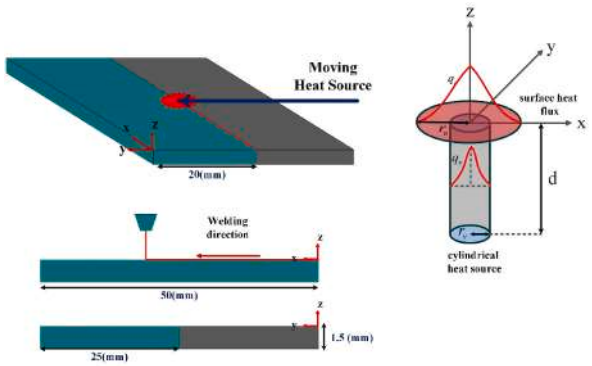

Fig. 2. A diagram of the laser welding process and its thermal energy model.

melt and the formation of a vapor column, termed the keyhole. By directly imparting energy to the material while minimizing heat transfer, this approach optimizes the depth of the weld. A cylindrical heat flux model was employed to accurately estimate the absorbed energy within the material. Consequently, the vapor column was disregarded and replaced with the cylindrical heat source. The following assumptions underpin the governing equations for the numerical laser welding simulation [37,38].

- Melt flow was considered incompressible and laminar.
- The initial temperature was presumed to be 298 K.
- Plasma formed on the surface of the molten pool was disregarded.

Continuity equation:

$$\nabla.\left(\rho\vec{U}\right)=0 \tag{3}$$

Momentum equation:

$$\frac{\partial\left(\rho\vec{U}\right)}{\partial t}+\nabla.\left(\rho\vec{U}\vec{U}\right)=-\nabla\mathrm{p}+\nabla.\left(\mu\nabla\vec{U}\right)+\rho\vec{g}-\frac{\mu}{K}\left(\vec{U}\right) \tag{4}$$

Where K represents the Darcian resistance coefficient, μ denotes the dynamic viscosity, $\vec{g}$ signifies the gravitational acceleration vector, p symbolizes pressure, $\vec{U}$ represents the velocity vector, t is the temporal variable, and ρ corresponds to the density.

To ascertain the regions undergoing liquefaction and solidification processes, the liquid fraction was quantified utilizing the subsequent equation. During the phase transition from liquid to solid, or vice versa, the liquid fraction oscillates between the limiting values of 0 and 1. Consequently, by incorporating the liquid fraction into the momentum conservation equation, the force emanating from the material phase metamorphosis can be exerted The mushy zone constant, designated as D, characterizes the material under investigation and quantifies the degree of coexistence between the solid and liquid phases during the solidification or melting processes [39].

$$K=\frac{f_L^3+c}{D(1-f_L)^2} \tag{5}$$

$$f_L=\begin{cases}0 & T\le T_s\\ \dfrac{T-T_s}{T_l-T_s} & T_s<\ T<T_l\\ 1 & T\ge T_l\end{cases} \tag{6}$$

Energy equation:

$$\frac{\partial(\rho H)}{\partial t}+\nabla.\left(\rho\vec{U}H\right)=\nabla.(k\nabla T)+q_V \tag{7}$$

k is the thermal conductivity coefficient, H is the total enthalpy, T is the temperature.

4.2. Boundary conditions

The thermal flux traversing the boundary layer, elucidated by the mathematical formulation denoted as Equation (8), was employed to delineate the constraint imposed upon the superficial stratum of the laminar structures. The ensuing Equations (9) and

(10) expound upon the tangential stress exerted upon the surface of the workpiece, engendered by the gradient of surface tension forces, concomitantly elucidating the genesis of the Marangoni convective current within the liquefied pool [35,40].

$$k\frac{\partial T}{\partial \vec{n}} = -\varepsilon\sigma\left(T^4 - T_\infty^4\right) - h(T - T_\infty) + q_S \tag{8}$$

$$\mu\frac{\partial u}{\partial z} = -\frac{\partial \gamma}{\partial T}\frac{\partial T}{\partial x} \tag{9}$$

$$\mu\frac{\partial v}{\partial z} = -\frac{\partial \gamma}{\partial T}\frac{\partial T}{\partial y} \tag{10}$$

Where the emissivity coefficient symbolizes ε, the ambient temperature is denoted as T_∞, σ represents the Stefan–Boltzmann constant, h signifies the convective heat transfer coefficient, and γ is the surface tension parameter.

The thermal boundary conditionality contemplated for the lateral and inferior surfaces incorporates the convective mode of heat transmission and the radiative thermal energy dissipation to the encompassing environment:

$$k\frac{\partial T}{\partial \vec{n}} = -\varepsilon\sigma\left(T^4 - T_\infty^4\right) - h(T - T_\infty) \tag{11}$$

4.3. Computational domain

A computational domain model was established, as depicted in Fig. 3. To precisely model the thermal flux as the transient heat source traverses the welding zone at discrete temporal intervals, a finely discretized mesh was implemented in those regions. These domains are anticipated to exhibit the most acute temperature gradients. Conversely, regions more distal from the weld locus were represented by a coarser mesh discretization. To evaluate the grid independence, four distinct computational meshes were juxtaposed. Ultimately, the mesh comprising 910,000 elements was selected for the prescribed geometry.

In order to simulate the melting and solidification process of the fusion zone region, the enthalpy-porosity technique was used. In this technique, the solid-melt interface is not accurately traced. On the other hand, a quantity called liquid fraction, which represents the fraction of the volume of cells that are in liquid state and is related to all cells in the entire computational domain. It is defined that the Momentum equation is included in the last term (Eqs. (4)–(6)). The region where the liquid fraction is zero up to one is called the mushy region. The mushy zone acts as a porous medium where the amount of metal is solid and increases from zero to one if the metal is molten. In Fig. 4, the effect of the melting and solidification model is observed. As can be seen in this figure, due to the phase change of the material and zero liquid fraction, the fluid velocity is 0 m/s in the fusion line. On the other hand, the melt flow velocity at the specified location in the figure is between 0.052 and 0.065 m/s.

5. Results and discussion

The findings of the laser welding experiments for two different types of stainless steel composed of austenitic and ferritic stainless steel joined with AISI 1060 steel base on the CCD experimental design are outlined in this section. The clear comparison between austenitic and ferritic material from microstructural changes, chemical composition and mechanical characterization is this study main propose. The influence of welding process variables like laser power, movement speed of welding, nozzle distance from the focal point position, and deviation of the beam position on the temperature fluctuation at the region adjacent to the melt pool boundary with base metals, the weld penetration depth and the joint tensile strength was thoroughly examined through statistical analysis. Additionally, the microstructural and micro-hardness analysis of the weld joints from fusion zone to the base metals of both materials for different laser welding configurations were evaluated.

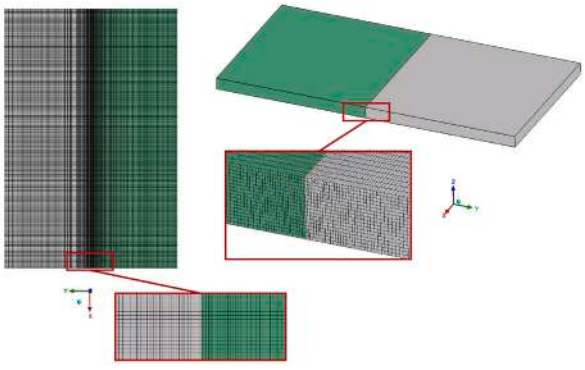

Fig. 3. Structured grids.

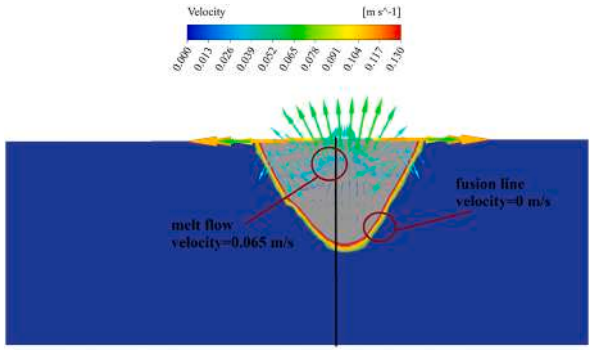

Fig. 4. Modeling the solidification process of the fusion zone region.

Table 5
ANOVA results for the temperature of AISI 304 near melt pool region.

Source	DF	Adj SS	Adj MS	F-Value	P-Value
Model	12	87522.6	7293.5	16.70	0.000
Linear	4	80771.2	20192.8	46.23	0.000
Power (W)	1	59700.4	59700.4	136.68	0.000
Speed (mm/min)	1	13395.4	13395.4	30.67	0.000
Focal distance (mm)	1	7.0	7.0	0.02	0.901
Deviation (mm)	1	7668.4	7668.4	17.56	0.001
Square	2	4064.0	2032.0	4.65	0.026
Focal distance (mm) × Focal distance (mm)	1	772.9	772.9	1.77	0.202
Deviation (mm) × Deviation (mm)	1	3677.3	3677.3	8.42	0.010
2-Way Interaction	6	2687.4	447.9	1.03	0.444
Laser Power (W) × welding Speed (mm/min)	1	885.1	885.1	2.03	0.174
Laser Power (W) × Focal distance (mm)	1	390.1	390.1	0.89	0.359
Laser Power (W) × Deviation (mm)	1	7.6	7.6	0.02	0.897
welding Speed (mm/min) × Focal distance (mm)	1	1.6	1.6	0.00	0.953
welding Speed (mm/min) × Deviation (mm)	1	1350.6	1350.6	3.09	0.098
Focal distance (mm) × Deviation (mm)	1	52.6	52.6	0.12	0.733
Error	16	6988.9	436.8		
Lack-of-Fit	12	5254.1	437.8	1.01	0.551
Pure Error	4	1734.8	433.7		
Total	28	94511.4			
S R-sq R-sq (adj) R-sq (pred)					
20.89 92.61 % 87.06 % 69.11 %					

5.1. The temperature fluctuation near the melt pool region influenced by the parameters of laser welding

The temperature measurements obtained from thermocouples near the melt pool were subjected to analysis of variance (ANOVA), and the corresponding results are presented in Table 5. The findings highlight the significant influence of welding velocity and laser power on the temperature fluctuations in the vicinity of the 304 stainless steel at distance of 2 mm from the center of the weld fusion zone. Among the parameters that have mutual effects on each other, the interaction between laser beam deviation and welding movement speed has had significant effect on the temperature variation at the region near the border of the austenitic 304 stainless steel base metal with the melt pool. The regression of the measured temperature of austenitic stainless steel 304, shows the relation

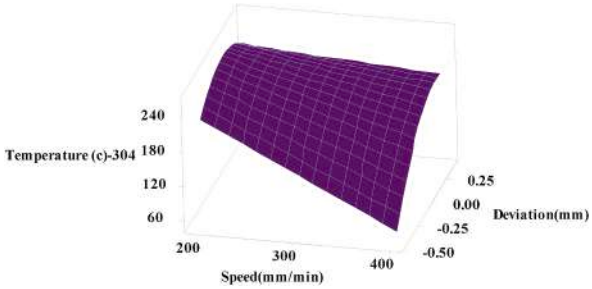

Fig. 5. Welding speed and beam deviation effect on AISI 304 temperature field.

between laser welding process parameters. It includes quadratic terms of the main parameters, non-linear terms of the mutual effect and interaction of the parameters on each other. Equation (12) illustrates the correlation between various parameters and the temperature measured around the molten pool. With an Rsq of 92 % and a lack of fit of 0.5, it can be inferred that the regression model closely correlates with the experimental data.

Temperature (AISI 304) = -535 + 2.285 Pow(W)+0.594 SP(mm/min)+ 79.3 FD(mm)-

126Dev(mm)5.29FD(mm) × FD(mm)- 288.5 Dev(mm) × Dev(mm)- 0.00297 Pow(W) ×

SP(mm/min)- 0.099 Pow(W) × FD(mm)- 0.069 Pow(W) × Dev(mm)- 0.006 SP(mm/min) ×

FD(mm)+ 0.919 SP(mm/min) × Dev(mm)- 9.1 FD (mm) × Dev (mm) (12)

Fig. 5 illustrates how the temperature surrounding the molten pool of 304 stainless steel is influenced by laser beam deflection and welding speed. With the increase in the laser beam movement speed, the measured temperature near the melt pool has decreased. When the laser beam is deflected towards the AISI 1060 steel, the highest rate of temperature decrease about a quarter of highest temperature range is observed. The decline in the temperature surrounding the melt pool, from 240 °C to 70 °C, can be observed clearly as the welding speed is increased. By transferring the laser beam to 304 steel and as a result of increasing the welding speed, there is no significant change (less than 15 percent) in the temperature reduction rate. It can be concluded that by deviation of laser beam toward AISI 1060 steel and higher thermal conductivity of 49.8 W/m.K versus 16.2 W/m.K, the reduction rate of temperature gradient has been evidently higher. Interestingly, there is a clear correlation between the temperature gradient and thermal conductivity coefficient (about a third for the measured temperature and thermal conductivity) when the laser beam position transferred to the AISI 1060 steel side. The low amount of thermal conductivity of 304 stainless steel resulted in minor effect on increasing welding speed that has not been notably changed.

The temperature of AISI 1060 steel is influenced by speed of beam movement and deviation of the beam, as depicted in Fig. 6. When the laser beam deviated toward AISI 1060 steel, the temperature range varied about 10 percent which is negligible in comparison with the measured temperature reduction of 304 stainless steel. In case of beam deviation in direction of 304 austenitic steel, the temperature reduced and has become half of the maximum temperature. It can be concluded that due to the lower thermal conductivity of 304 stainless steel, the temperature reduced at low speed and thereby the measured temperature is evidently higher when the laser deviated toward austenitic stainless steel. By welding at the center line of the weld joint, the maximum measured temperature is observed on both AISI 1060 steel and 304 austenitic AISI 1060 steel particularly at higher welding speed.

Table 6 illustrates the outcomes of variance analysis for the temperature fluctuations at adjacent region of the molten pool during welding of AISI 1060 steel and AISI 420 stainless steel. The ANOVA findings demonstrate that temperature changes at distance of 2 mm from the fusion zone center line on 420 ferritic stainless steel are primarily influenced by laser power, laser beam deviation and welding speed. The temperature changes have been significantly influenced by the interaction between the laser beam deviation and beam linear speed, among other parameters that have a mutual effect on each other. The regression equation of measured temperature of 420 stainless steel involves non-linear, quadratic and interaction terms of the parameters. Equation (13) shows the relationship of the parameters with the measured temperature.

Temperature (AISI 420) = −746 + 2.513 Pow (W) + 1.49 SP (mm/min) +107.0 FD(mm)-164 Dev(mm)- 0.00108 SP(mm/min) × SP (mm/min)- 6.20 FD(mm) × FD(mm)- 311 Dev(mm) × Dev (mm)- 0.00325 Pow(W) × SP(mm/min)- 0.122 Pow(W) × FD(mm)- 0.325 Pow(W) × Dev(mm)- 0.048

SP(mm/min) × FD(mm)+ 1.225 SP(mm/min) × Dev (mm)- 2.5 FD (mm) × Dev (mm) (13)

Fig. 7 illustrates the impact of variations in laser power and laser beam deviation on the temperature fluctuations surrounding the melt pool of 420 stainless steel. An increase in laser power from 250 to 400 W, along with irradiation of the junction of two parts, led to a temperature rise of around 180 °C. When the laser beam deviated toward AISI 1060 STEEL, it created lower temperature changes than the center of two parts. Consequently, it can be inferred that. the interaction between laser power and beam deviation have influenced the temperature when the laser beam is irradiated the 420 stainless steel with beam deflection on that. It can be seen that

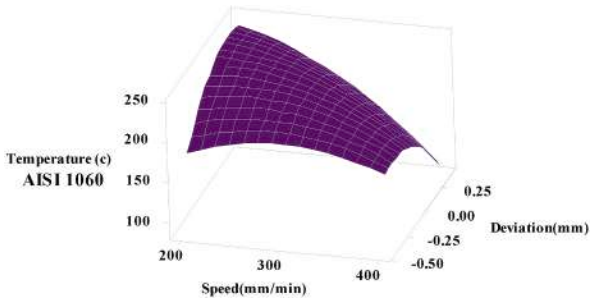

Fig. 6. Beam deviation and welding speed effect on the temperature of AISI 1060 steel.

Table 6
ANOVA results for the temperature near the melt pool of AISI 420.

Source	DF	Adj SS	Adj MS	F-Value	P-Value
Model	13	95377	7336.7	16.00	0.000
Linear	4	86394	21598.5	47.10	0.000
Power (W)	1	65940	65940.2	143.81	0.000
Speed (mm/min)	1	14308	14308.2	31.20	0.000
Focal distance (mm)	1	2	1.5	0.00	0.955
Deviation (mm)	1	6144	6144.0	13.40	0.002
Square	3	4662	1554.1	3.39	0.046
Speed (mm/min) × Speed (mm/min)	1	196	196.1	0.43	0.523
Focal distance (mm) × Focal distance (mm)	1	1034	1034.2	2.26	0.154
Deviation (mm) × Deviation (mm)	1	4171	4170.5	9.10	0.009
2-Way Interaction	6	4321	720.1	1.57	0.223
Power (W) × Speed (mm/min)	1	1056	1056.3	2.30	0.150
Power (W) × Focal distance (mm)	1	600	600.3	1.31	0.270
Power (W) × Deviation (mm)	1	169	169.0	0.37	0.553
Speed (mm/min) × Focal distance (mm)	1	90	90.2	0.20	0.664
Speed (mm/min) × Deviation (mm)	1	2401	2401.0	5.24	0.037
Focal distance (mm) × Deviation (mm)	1	4	4.0	0.01	0.927
Error	15	6878	458.5		
Lack-of-Fit	11	3449	313.6	0.37	0.916
Pure Error	4	3429	857.2		
Total	28	102255			
S R-sq R-sq (adj) R-sq (pred)					
21.4134 93.27 % 87.44 % 78.38 %					

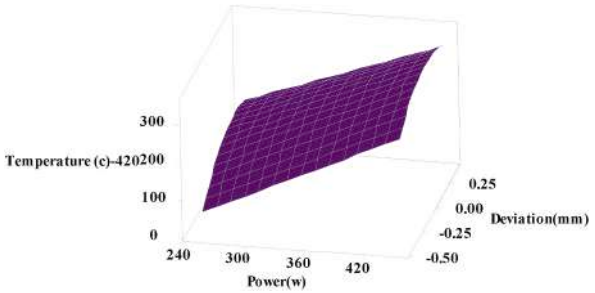

Fig. 7. The influence of the laser power and deviation of the laser beam on AISI 420 temperature variation.

the temperature changes according to the laser power changes under linear trend for all three locations of laser beam irradiation. In general, when the laser beam is deflected towards 420 stainless steel, the higher temperature level is observed. According to the higher amount of 420 stainless steel thermal conductivity of stainless steel about 24.9 W/m.K than 304 stainless steel, the variation of AISI 420 temperature by deviation of laser beam was lower than austenitic stainless steel.

The effect of incident laser beam power and deviation of the laser beam position on temperature variation near the melt pool of AISI 1060 STEEL joined with AISI 420 is observed in Fig. 8. According to Fig. 8, increasing laser power has had an incremental trend of AISI 1060 STEEL temperature which is similar for deviation toward both materials. By laser welding at the center of weld joint, the maximum temperature for AISI 1060 STEEL is gained. At high level of laser power, by deviating laser beam to the 420 stainless steel side, the higher temperature of AISI 1060 STEEL is observed due to higher melt volume of 420 stainless steel. At low level of laser

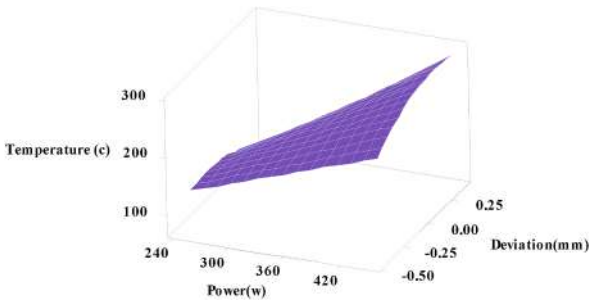

Fig. 8. The influence of incident laser power and deviation of the beam on AISI 1060 steel temperature joined with AISI 420.

power about 250 W, by displacement of laser beam incident position to the 420 stainless steel workpiece, the AISI 1060 steel temperature clearly reduced due to insufficient melting of two materials and more distance of laser beam and thermocouple tip.

5.2. Investigating the parameters impact on tensile strength of the dissimilar joint

Table 7 illustrates the results of the ANOVA performed on the laser welding variables that impact the tensile strength of AISI 1060 steel and stainless steel 420 dissimilar welds. Table 7 presents the findings of the ANOVA analysis performed on the welding factors by laser affecting the tensile strength of dissimilar 420 stainless steel and AISI 1060 steel.

The parameters examined include laser power, beam moving speed, focal distance and laser beam deviating in direction of each material. It can be seen that beam power, welding movement speed and beam deviating had the notable impact on tensile strength of the joint. The interplay between the deflection of the beam and its incident power has the most significant impact on the tensile strength. A high Rsq value of 97.9 % and Lack of Fit value of 0.408 suggest that the regression equation aligns closely with the experimental results. equation (14) includes square of the parameters, non-linear and linear terms as presented for the tensile strength.

$$\text{Tensile strength (S.S 420)} = -41 + 2.067\ \text{Pow (W)} - 0.6583\ \text{SP (mm/min)} + 32.7\ \text{FD (mm)} + 527\ \text{Dev (mm)} + 0.96\ \text{FD (mm)} \times \text{FD (mm)} + 233.4\ \text{Dev (mm)} \times \text{Dev (mm)} - 0.1250\ \text{Pow (W)} \times \text{FD(mm)} - 1.563\ \text{Pow (W)} \times \text{Dev (mm)} + 0.325\ \text{SP(mm/min)} \times \text{Dev (mm)} - 47.5\ \text{FD (mm)} \times \text{Dev (mm)} \quad (14)$$

The influence of beam deflection and power of the laser beam on the tensile strength of AISI 1060 steel in combination with 420 stainless steel is depicted in Fig. 9. The relationship between changes in laser power and deviation of the laser beam changes toward each material on tensile strength changed linearly. When the beam power rises from 250 to 400 W, by laser beam deflection towards AISI 1060 steel, the tensile strength has increased by about 220 MPa. By moving position of the laser beam to the junction of the AISI 1060 steel and austenitic steel and also ferritic stainless steel, the rate of increase of the tensile strain is 150 MPa. Therefore, the highest tensile strength is obtained by irradiating AISI 1060 steel with a laser beam at a power of 400 W. Due to the failure of the sample from the weld joint or AISI 1060 steel side, the AISI 1060 steel tensile strength and the melt pool depth variation in the AISI 1060 steel is the major measurement to determine the weld joint tensile strength.

Fig. 10 depicts the influence of the beam power and its deflection on AISI 1060 steel and 304 stainless steel joint tensile strength.

The correlation between alterations in laser power and adjustments in tensile strength is directly proportional when contrasted with the fluctuation in tensile strength due to deviation. An increase in laser power from 250 to 400 W resulted in an increase of 200 MPa in the tensile strength of the welded joint.

By directing the beam irradiation position towards the weld bead joint center and the austenitic stainless steel side up to (+0.5 mm), the occurrence of excessive reduction in the tensile strength rate is effectively minimized. By beam deviating toward AISI 1060 steel, the tensile strength slightly increased compared to the center of the weld joint. This could be due to the higher melting of AISI 1060 steel and more participation of that for composition in fusion zone by austenitic stainless steel. Clear comparison of the tensile strength in dissimilar joint with 304 austenitic stainless steel and 420 ferritic stainless steel shows higher tensile strength variation. It can be said that beam deviation toward AISI 1060 steel can improve the tensile strength of the joint more effectively in comparison to 304 stainless steel. Changes in temperature gradient near AISI 1060 steel can create more temperature gradient and reduce porosity formation near the fusion line of AISI 1060 steel. According to Fig. 11, deviating laser beam position in direction of AISI 1060 steel created depth of melt pool more than 1 mm. On the contrary, when the laser beam deviated toward 304 stainless steel, the depth of the melt pool increased progressively as the laser power was enhanced. the volume of the melted material increased. The correlation

Table 7
The results of ANOVA for tensile strength of the AISI 420 and AISI 1060 steel joint.

Source	DF	Adj SS	Adj MS	F-Value	P-Value
Model	10	194241	19424	85.82	0.000
Linear	4	185688	46422	205.09	0.000
Power (W)	1	147267	147267	650.63	0.000
Speed (mm/min)	1	26004	26004	114.89	0.000
Focal distance (mm)	1	267	267	1.18	0.292
Deviation (mm)	1	12150	12150	53.68	0.000
Square	2	2409	1204	5.32	0.015
Focal distance (mm) × Focal distance (mm)	1	25	25	0.11	0.741
Deviation (mm) × Deviation (mm)	1	2406	2406	10.63	0.004
2-Way Interaction	4	6144	1536	6.79	0.002
Power (W) × Focal distance (mm)	1	625	625	2.76	0.114
Power (W) × Deviation (mm)	1	3906	3906	17.26	0.001
Speed (mm/min) × Deviation (mm)	1	169	169	0.75	0.399
Focal distance (mm) × Deviation (mm)	1	1444	1444	6.38	0.021
Error	18	4074	226		
Lack-of-Fit	14	3379	241	1.39	0.408
Pure Error	4	695	174		
Total	28	198315			
S R-sq R-sq (adj) R-sq (pred)					
15.0447 96 % 93.8 % 97.9 %					

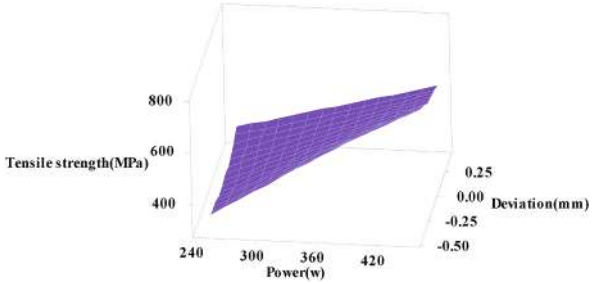

Fig. 9. Influence of power of the laser beam and beam deviation on tensile strength of AISI 1060 and AISI 420 joint.

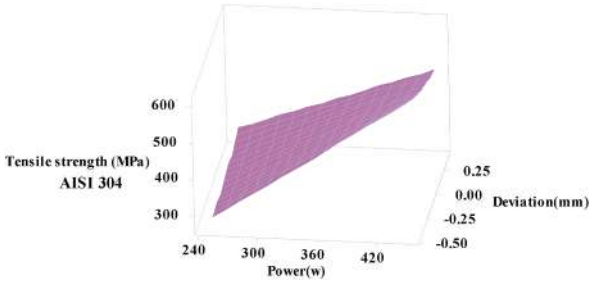

Fig. 10. Effect of beam deviation and laser power on the tensile strength of AISI 1060 and AISI 304.

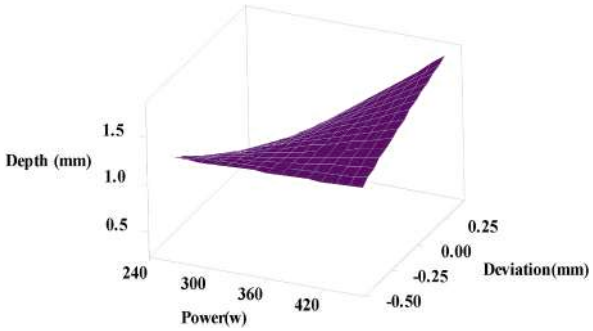

Fig. 11. Effect of deviating the laser beam position and laser power on melt pool depth for AISI 1060 and AISI 304.

between the tensile strength of 304 stainless steel and AISI 1060 steel is directly influenced by the volume of melted material, specifically the depth of penetration. In other words, more weld penetration produces higher tensile strength. Based on Fig. 11, the beam position deviating toward the AISI 1060 steel side resulted in increased weld depth and additional tensile strength.

5.3. Microstructural analysis

The microstructural analysis of ferritic stainless steel with AISI 1060 steel weld joint from base metals to the fusion zone is observed in Fig. 12. In general, the bulk of fusion zone microstructure composed of ferritic 420 stainless steel transformation. As shown in Fig. 12a and c, AISI 420 stainless steel base metal microstructure consists of globular carbides randomly dispersed in a ferrite matrix. Fig. 12 b and 12d shows the martensitic microstructure of AISI 1060 base metal.

As depicted in Fig. 12a, remarkable grain coarsening at the HAZ region of ferrite steel is clearly observed which in turn will decrease the toughness of ferritic and martensitic stainless steels at high temperatures due to phase transformation as reported in Ref. [41]. The narrow region of heat affected zone (HAZ) composed of coarse grain ferrite which created because of fast cooling and lower heat input rate of the welded joints [41]. The coarse ferrite grains and grain boundary at HAZ region have been created because of the incomplete transformation of primary ferrite grains into austenite at high temperatures and remaining within the structure to cool down. Additionally, it is clearly seen in Fig. 12c that quantity and dimensions of carbides near the HAZ have been decreased due to high temperatures gradient created from fusion zone to the base metal.

Furthermore, some welding defects such as porosities is observed adjacent to the AISI 1060 base metal that could result in clear reduction in mechanical strength of the weld joint as reported in Ref. [30].

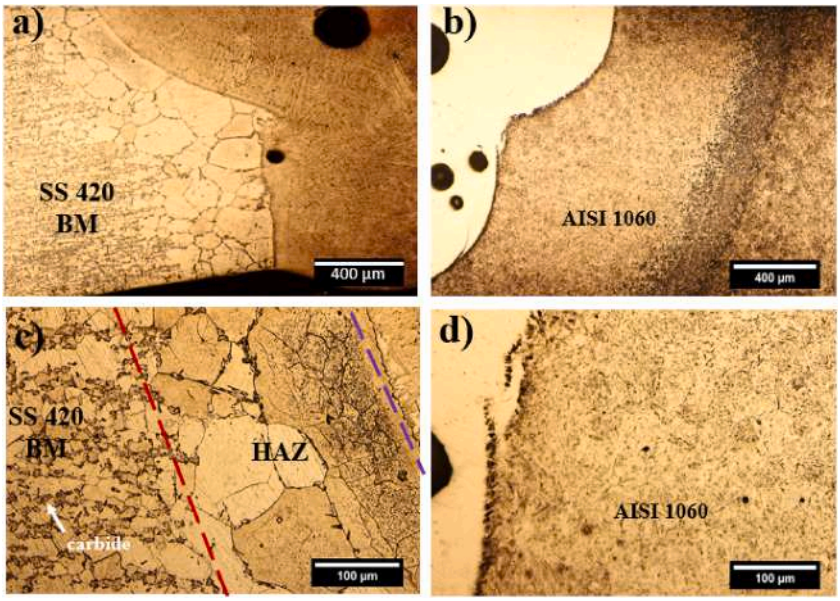

Fig. 12. The microstructure variation of the weld joint at laser power of 400 W, welding speed of 250 mm/min for a) AISI 420 base metal and fusion zone, b) AISI 1060 base metal and fusion zone, c) HAZ of AISI 420, d) HAZ of AISI 1060.

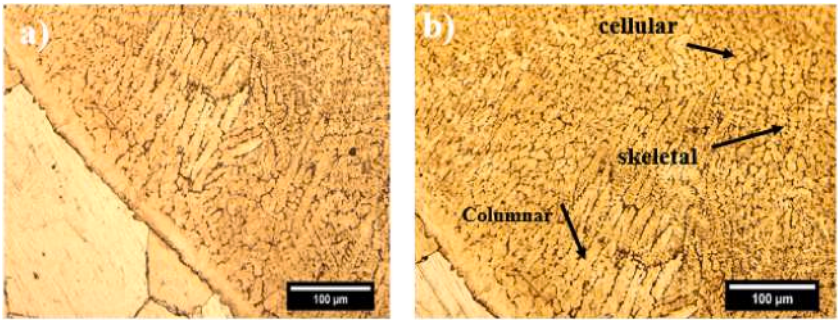

Fig. 13. Weld fusion zone microstructure of AISI 420 stainless steel and AISI 1060 at a) fusion line of AISI 420, b) center of fusion zone.

After laser heating process, the cooling process started and delta ferrite has been the first structure formed at solidification process. Afterward austenite has been formed by transformation from delta ferrite at cooling process. When the temperature cools down to the room temperature, the austenite transforms into martensite microstructure. As it is seen at Fig. 13, the fusion zone composed of mixture of martensite and delta ferrite phase due to rapid cooling cycle in laser welding process. At fusion boundary zone, the microstructure consists of columnar dendrites and skeletal columnar ferrite. At the center of fusion zone, a cellular-type structure is seen over dendritic as a result of higher thermal gradient than cooling rate. The microstructure of AISI 1060 composed of martensite microstructure and a major part of microstructure composed of AISI 420 stainless steel.

In contrast to AISI 1060, the austenitic stainless steel 304 has lower thermal conductivity coefficient and lower melting point. This results in the formation of the majority of the fusion zone from austenitic stainless steel, consisting of ferrite and austenite phases, as illustrated in Fig. 14. The AISI 304 microstructure composed of the austenitic grains with stringers of ferrite δ. As it is observed in Fig. 14b and c, at the fusion boundary zone, dendritic structure which is mainly formed from skeletal and columnar ferrite in austenite matrix is observed. Due to rapid cooling and insufficient time of complete transformation, a remarkable part of skeletal delta-ferrite and dendritic microstructure at austenite matrix has composed of fusion zone microstructure.

5.4. The temperature field results

A clear comparison was performed to assess the effect of laser welding parameters on the temperature field variation for both joint configurations of AISI 1060 with AISI 304 and AISI 420.

Fig. 15 shows the temperature distribution at the AISI 1060/420 joint top surface for different welding speeds at laser power of 300 W. At low laser welding speeds and high-power densities, there is a possibility of surface evaporation on the molten pool and partial

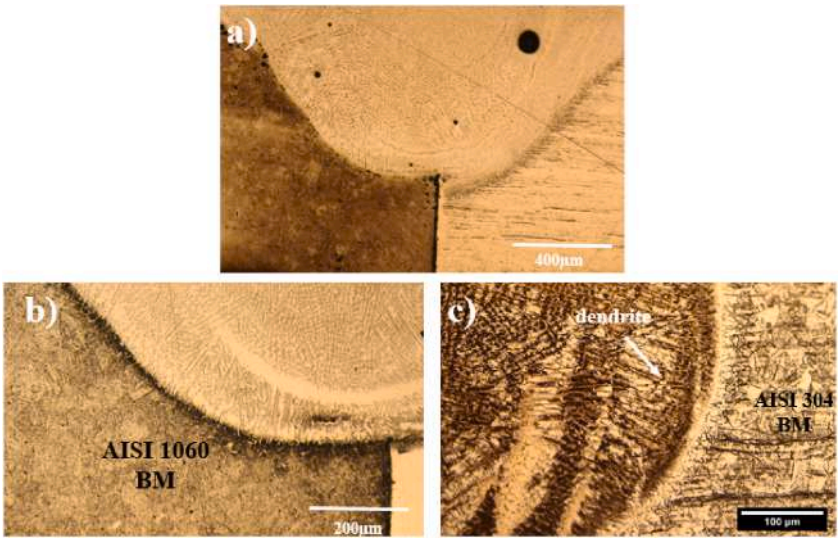

Fig. 14. Weld fusion zone microstructure of AISI 304 stainless steel and AISI 1060 at a) weld fusion zone, b) fusion zone adjacent to AISI 1060, c) fusion zone adjacent to AISI 304.

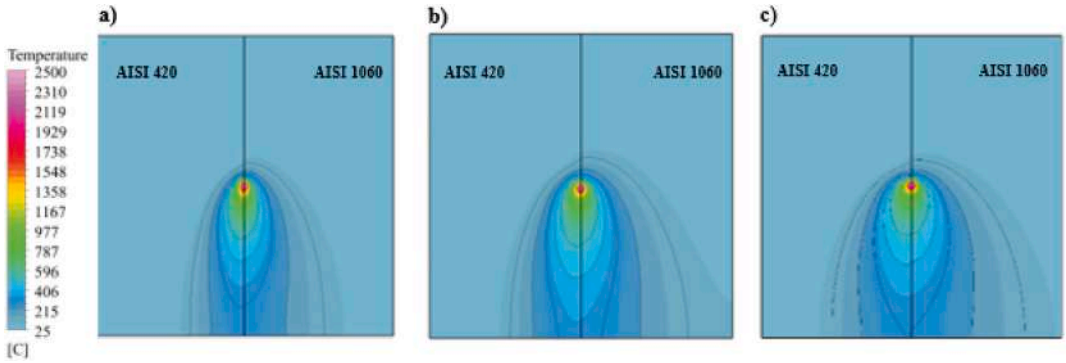

Fig. 15. Comparison of temperature field for AISI1060/420 joint at laser power of 350 W and different welding speed of a)150 mm/min, b)250 mm/min, c)300 mm/min.

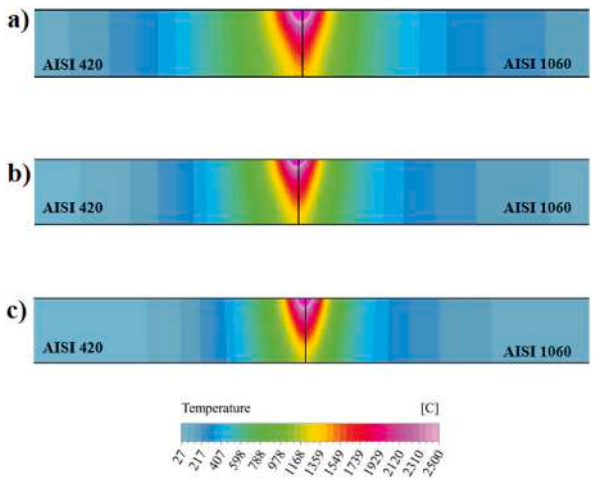

Fig. 16. The cross section temperature field of AISI420/AISI1060 joint at different welding speed of a)150 mm/min, b)250 mm/min, c)300 mm/min.

keyhole development. At laser power more than 300 W and welding at focal point position the laser beam energy density reached to the value of 0.044 MW/cm^2, the possibility of keyhole formation existed. In this study, the energy received in the workpiece was modeled using a mix of surface and volume heat flux. The crucial aspect of this thermal model is to take into account the evaporation conditions of the material on the surface of the part, without including the modeling of the vapor phase of the material.

By increasing the welding speed, the high temperature region with amount of higher than 700 °C clearly reduced when the welding speed increased from 150 to 300 mm/min. At welding speed of 250 mm/min, the high temperature region extended more compared to the other conditions because of having enough time for laser beam irradiation with workpiece surface. On the other hand, slow welding speed can induce higher melting regional volume at the position of beam irradiation and thereby will limit more heat dissipation toward welded plates. Therefore, at moderate speed of 250 mm/min, the heat dissipation and efficient melt volume had been maximum while at welding speed of 300 mm/min, the heat dissipation reduced remarkably due to receiving lower heat input at time unit.

The temperature distribution at cross section of welded sample is illustrated in Fig. 16. According to the increasing the welding speed, at low welding speed of 150 mm/min, the high temperature region (the temperature higher than 1300 °C) extended more at 420 stainless steel side due to the lower thermal conductivity coefficient and extension of melted volume at AISI remarkably increased more than AISI 1060 steel (see Fig. 16a). On the other hand, as it is observed in Fig. 16b and c, the temperature dissipation at AISI 1060 steel side was clearly more than 420 stainless steel because of higher thermal conductivity rate about twice of 420 stainless steel. Therefore, the melted region at both depth and width of the weld joint is clearly bigger at 420 stainless steel side while the heat dissipated more at AISI 1060 side and lower melting volume was created at AISI 1060 side although the melting point of AISI 1060 is lower about 200 °C.

Fig. 17 illustrates a clear comparison between the cross section temperature field predicted by numerical simulation and experiments. It is clearly observed that melt pool area is vividly bigger at 420 stainless steel side with smaller heat affected zone compared to the AISI 1060 heat affected area. Additionally, Fig. 17 illustrates the melt pool shape and thereby keyhole formation at laser power of 350 W, beam diameter of 1 mm which keyhole formation clearly observed for AISI420/AISI 1060 joint configuration. Unlike heat conduction welding, the metal vapor is created in addition to the metal melt. This vapor partially displaces the melt and thereby leading to the creation of keyhole. Apart from the melt pool region, the heat affected zone of AISI 1060 seems to be extended more than 420 stainless steel because of having lower melting point and low tempering temperature changed the martensitic to tempered martensitic microstructure at the heat affected zone area. At the 420 stainless steel side, the coarse grain area created at the temperature higher than 500 °C while the microstructural changes took occurred for AISI 1060 at the temperature higher than 300 °C.

Fig.18a–c illustrates the effect of welding speed on the temperature distribution at the fusion zone region which generally investigate the high temperature region. By reducing the welding speed, both width and penetration depth of high temperature region (more than 1700 °C) increased remarkably. It is evidently observed that the penetration rate rose at higher rate and the depth of the region with temperature higher than 2000 °C remarkably increased. Therefore, it can be concluded that the high temperature region is in direct relation with amount of unit energy absorption and thereby keyhole formation at welding speed of 150 mm/min and laser power of 350 W has more possibility particularly by increasing the depth of melted region at the temperature higher than 1700 °C (see Fig. 18c).

The temperature distribution at weld joint cross section is observed at Fig. 19. By increasing the laser power both melt pool depth and width significantly increased. The extension of melt pool and heat affected zone regions toward AISI 304 were evidently higher compared to AISI 1060 steel as shown in Fig. 19a–c. Higher thermal conductivity of AISI 1060 steel (about 3 fold of AISI 304) and almost near melting point of both alloys resulted in creating smaller melt volume and heat affected region compared to the 304 stainless steel due to dissipation a considerable amount of energy via higher heat transfer rate of AISI 1060 steel. the lower heat transfer rate and thereby accumulation of heat at the melt pool region resulted in bigger melt pool and heat affected one region. Fig. 20 depicts a clear comparison between the numerical and experimental investigation of melt pool geometry for AISI 304/AISI 1060 joint. The temperature gradient at cross section of the workpiece is shown in Fig. 20a. The simulation result of the melt pool flow depicted in

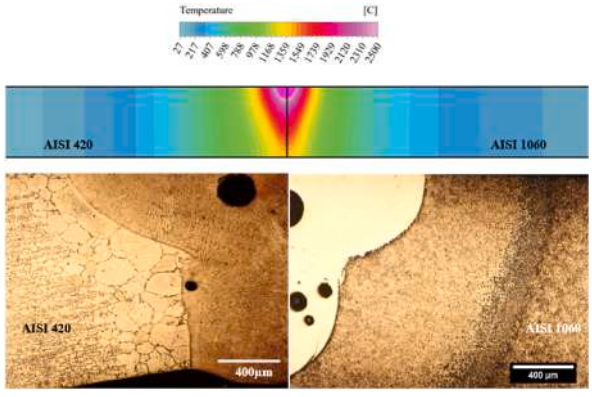

Fig. 17. Comparison between numerical simulation of temperature field with experimental results AISI420/AISI1060 joint at laser power of 350 W and welding speed of 150 mm/min.

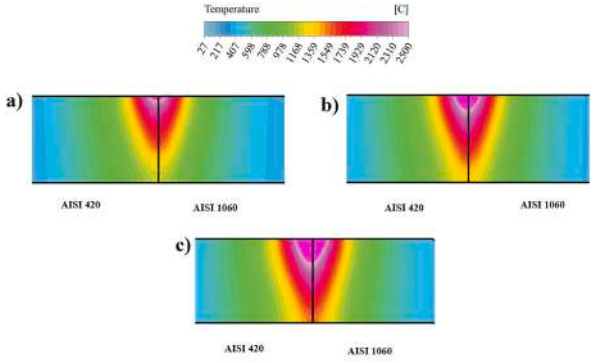

Fig. 18. The numerical simulation results for the contour of high temperature region for laser power of power of 350 W and different welding speed of a)300 mm/min, b)250 mm/min, c)150 mm/min.

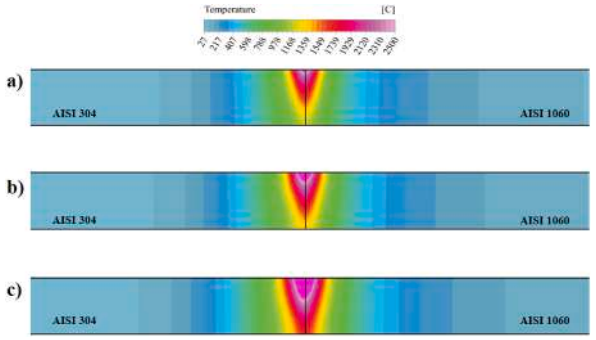

Fig. 19. The cross section temperature field of AISI 304/AISI 1060 joint at welding speed of 250 mm/min and different laser power of a)250 W, b) 350 W, c)450 W.

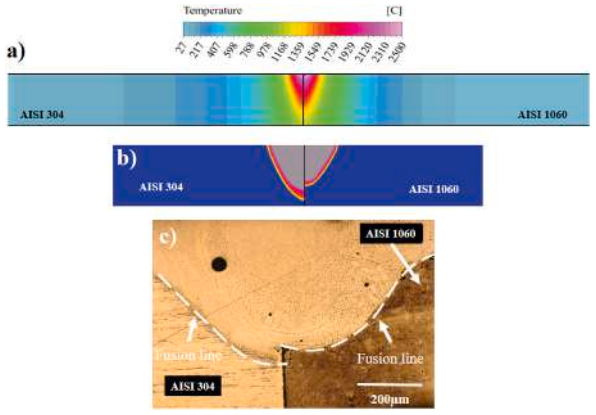

Fig. 20. The cross section temperature field of AISI 304/AISI 1060 joint at welding speed of 250 mm/min and laser power of a) The temperature field, b) simulated melt flow, c) actual melt pool region.

Fig. 20b and implies that the melt pool penetration depth is clearly larger at AISI 304 side compared to AISI 1060 steel. On the other hand, the melt pool experimental results shown in Fig. 20c and implies the melt pool penetration depth at AISI 304 is slightly more than AISI 1060 side.

Fig. 21 illustrates the effect of increasing the laser power on the temperature distribution and heat dissipation from the top surface of the workpiece. It was evidently observed that the temperature dissipated at the higher speed and wider region toward AISI 1060 side due to the higher thermal conductivity rate and lower melting point. By considering the temperature gradient variation from Fig.21a–c, in case the laser power increased from 250 to 450 W, the wider region at low temperature is observed at AISI 1060 side while the high temperature region did not show a considerable difference.

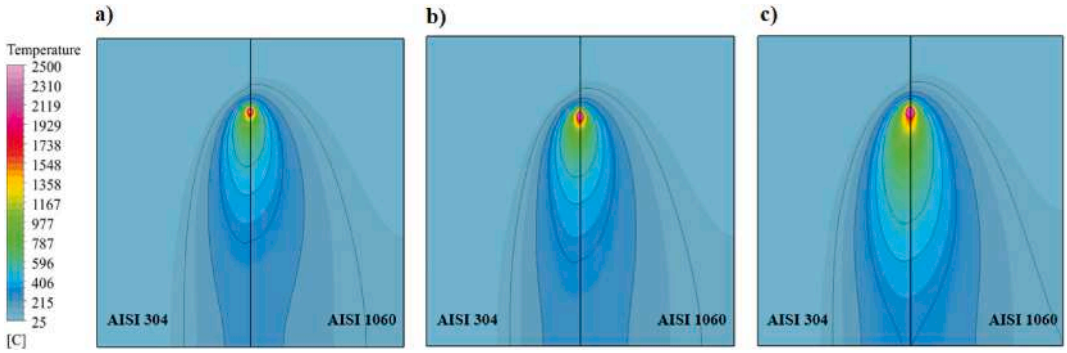

Fig. 21. The cross section temperature field of AISI 304/AISI 1060 joint at welding speed of 250 mm/min and different laser power of a)250 W, b) 350 W, c)450 W.

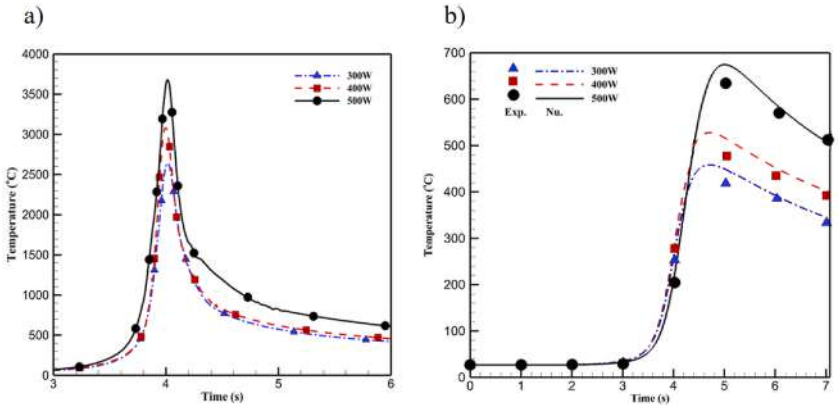

Fig. 22. The temperature history for a) simulation results, b) Experimental and simulation results comparison.

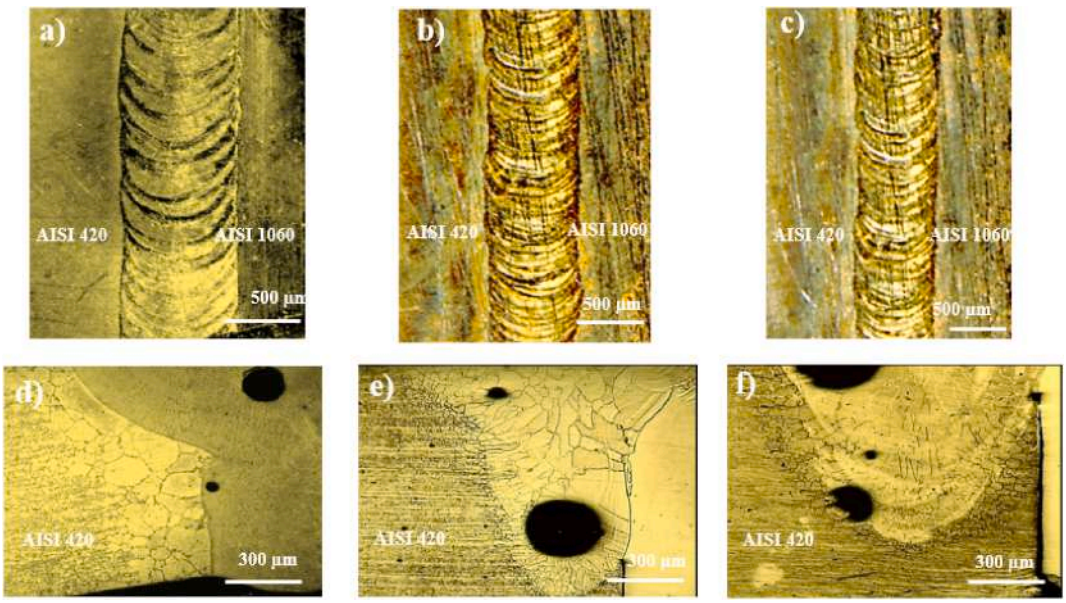

Fig. 23. Weld bead surface morphology for different welding speeds of a) 150 mm/min, b)250 mm/min, c)300 mm/min and related melt pool shape for welding speed of d) 150 mm/min, e) 250 mm/min, f) 300 mm/min.

Fig. 22a shows the temperature history at the center of the melt via numerical simulation results when the laser power increased from 300 to 500 W. By increasing the laser power, the maximum temperature increased about 1000 °C which is about 45 percent of total temperature. According to the numerical simulation results, the phenomenon of melting and thereby solidification took occurred in at short time less than 1 s.

Fig. 22b clearly illustrates a comparison between experimental and numerical results at distance of 2 mm from the center of the melt pool (weld bead center) where the thermocouples are placed and no phase transformation (e.g melting and solidification) took occurred at this region. The numerical simulation results are in good agreement with experimental data. The temperature history data at Fig. 22b shows a gradual reduction rate from the average (500–300 °C). The slop of center point temperature is significantly steeper than 2 mm region.

The weld bead appearance according to the different laser welding speed levels is observed in Fig. 23a–c. Generally, the weld bead appearance seems to be coarser with wider width at welding speed of 150 mm/min compared to the higher welding speeds of 250 and 300 mm/min. By increasing welding speed from 150 to 300 mm/min the weld bead width clearly reduced about 30 percent.

At laser welding of 150 mm/min, the keyhole is formed while at welding speed of 300 mm/min the welding mode gradually transform from keyhole to conduction mode. On the other hand, it is vividly observed that by increasing the welding speed, more number of porosities with bigger size were formed. Apart from this, the majority of melt pool volume composed of AISI 420 steel although the laser beam irradiated at the dissimilar joint centerline. It can be concluded that by increasing the welding speed, the AISI 1060 melting efficiency vividly reduced as it is observed in Fig. 23d–f.

5.5. Comparison the microhardness profile of the joint

Fig. 24 shows the micro-hardness profile of laser welded samples cross section at depth of 0.4 mm from both base metals to the fusion zone. The average microhardness for AISI 304 and AISI 420 is about 220 and 420 Hv, respectively. At the HAZ of AISI 304, the microhardness gradually increased and thereby reached to the value about 550 Hv at the center of the fusion zone. From the center of the fusion zone onward, the microhardness clearly reduce and has had the value about 450 Hv at HAZ and base metal of AISI 1060 steel. For the AISI 420, the microhardness slightly reduced at HAZ region due to coarse grains and then increased to the value of 640 Hv at the center of the fusion zone. After that, the hardness clearly reduced and reached to the value about 500 Hv just after the fusion line of AISI 1060 steel. Due to high temperature gradient at the fusion boundary and also fast cooling rate induced by base metals, the microhardness values significantly increased from fusion boundary of AISI 304 and AISI 420 to the weld center line.

5.6. Fracture surface analysis of the joint

The dissimilar welded joints mechanical properties of 304 and 420 stainless steels with AISI 1060 steel were evaluated by examining the tensile strength, strain rate, and fracture cross-sectional area analysis. The joint failure mechanism was investigated by conducting three repetitions of each test, examining the impact of laser power and variation focal distance. Fig. 25 depicts the tensile tests samples appearance of welded samples at two levels of laser incident power for combination of both 304 and 420 stainless steel with AISI 1060 steel.

The images depicted in Fig. 26 are visible obtained from the fracture surface of the test samples of austenitic steel 304 and AISI 1060 steel illustrate that the fracture section of 304 steel has a ductile fracture and the depth of fracture dimples and cavities toward 304 stainless steel are higher than AISI 1060 steel (see Fig. 26a–h). Comparison the cross-section of AISI 1060 steel and austenitic stainless steel depicts that a series of dimples and cavities can be seen in the fracture section of 304 steel. In Fig. 26b, it is evident that as the laser power rises, the depth of the cavities also increases compared to Fig. 26a, which indicates more absorption of laser beam energy and more load in order to break the joint. Furthermore, comparison Fig. 26c and d implies that by increasing the focal distance, the cavities depth clearly reduced and the lower number of dimples and cavities are observed in Fig. 26d for AISI 304 steel surface failure.

Fig. 26f illustrates the remarkable increase of cavities fracture depth for AISI 1060 steel due to the higher laser power level. Therefore, it can be said that the rise in laser power leads to a boost in tensile strength and as a result, an increase in the depth of the

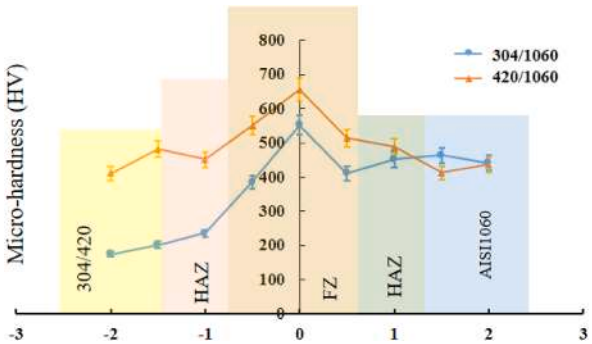

Fig. 24. Micro hardness profile of laser welded samples of dissimilar weld.

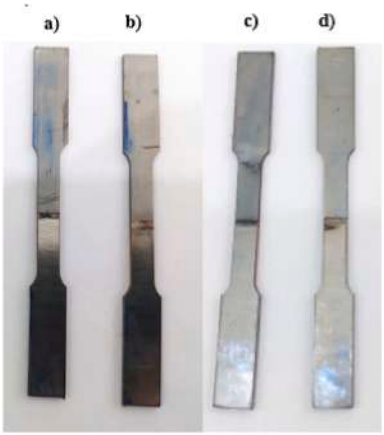

Fig. 25. Appearance of provided tensile tests samples of AISI 1060 steel with AISI 420 at laser power of a) 350 W, b) 450 W and with AISI 304 at laser power of c) 350 W, d) 450 W.

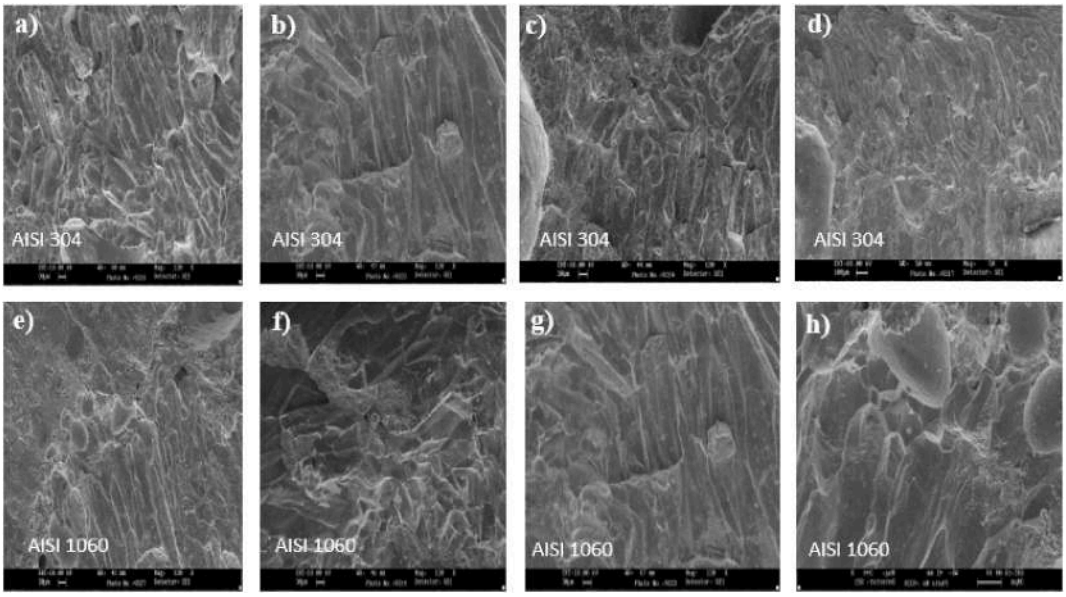

Fig. 26. The image of the fracture surface for 304 steel at laser power of a) 350 W, b) 450 W and focal distance of c) 0 mm, d) 4 mm at laser power of 400 W, AISI 1060 steel at laser power of e) 350 W, f) 450 W, and focal distance of g) 0 mm, h) 4 mm.

cavities and more energy for the fracture of the cross-section, which is caused by the ductile fracture mechanism in 304 steel and brittle fracture for AISI 1060 steel. Comparison the fracture surface appearance of Fig. 26h, inferred that, the higher focal length produces shallower cavities depth.

Fig. 27 shows the fracture section of AISI 1060 steel and 420 stainless steel. As can be seen in Fig. 27a, the fracture section of the AISI 420 has a smaller cavity depth than 304 steel. Although the tensile strength values are higher in the tensile test, it can be seen in Fig. 27e that the fracture surface of the material for AISI 1060 steel also indicates a brittle fracture mechanism. The depth of the cavities created at the AISI 1060 steel side of joint with AISI420 was clearly deeper than AISI 304 steel. The greater strength of ferritic stainless steel 420 in comparison to steel 304 results in a deeper formation of cavities on the fracture surface of the AISI 1060 steel when connected with 420 steel. This observation signifies the enhanced tensile strength of this particular joint. By augmenting the laser power from 350 to 450 W, the extent of the fracture surface cavities amplifies in both ferritic steel and AISI 1060 steel sections (see Fig. 27b and f). Fig. 27c and d depicts the effect of focal length on the fracture surface appearance. Fig. 27c shows deep cavities formed at 420 stainless steel side while the cavities depth reduced clearly as shown in Fig. 27d. On the contrary, the AISI 1060 has had a steeper depth as shown in Fig. 27g and slightly reduce as it is observed in Fig. 27h.

The tensile stress of two different joint configuration depicts different values of ultimate tensile stress and elongation values as shown in Fig. 28. Generally, the joint of AISI 420/1060 had higher tensile stress compared to the AISI 304/1060. On the other hand,

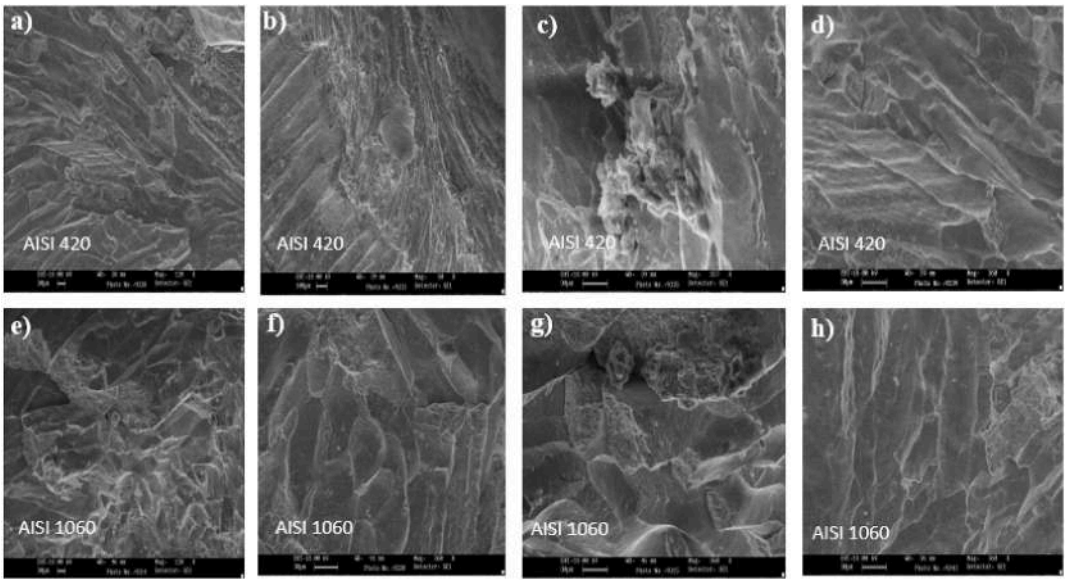

Fig. 27. The image of the fracture surface for 420 stainless steel at laser power of a) 350 W, b) 450 W and focal distance of c) 0 mm, d) 4 mm at laser power of 400 W and for AISI 1060 steel at laser power of e) 350 W, f) 450 W and focal distance of g) 0 mm, h) 4 mm.

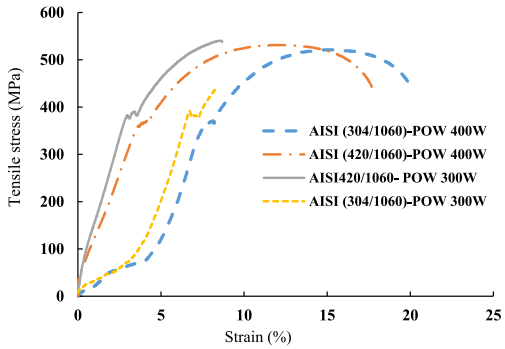

Fig. 28. Tensile stress diagram for different joints configuration of AISI 304/1060 and AISI 420/1060 at different laser power of 300 W, 400 W, welding speed of 200 mm/min.

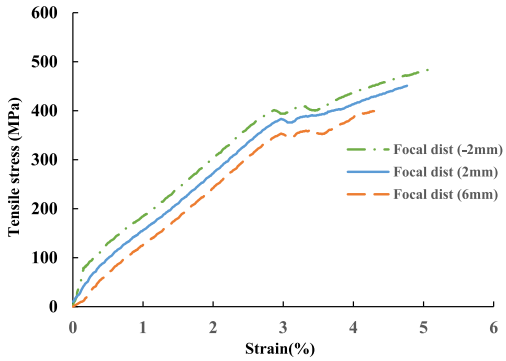

Fig. 29. Tensile stress diagram for AISI 420/1060 for the test condition with the laser power of 350 W, welding speed of 250 mm/min at different focal distances.

both joints elongation rate by increasing the laser power significantly augmented particularly for AISI 304/1060. The elongation rate at laser power of 300 W for AISI 420/1060 was about 40 percent of ultimate strain welding at laser power of 400 W. For AISI 304/1060 joint, the elongation rate for laser power of 300 W was about 30 percent of ultimate value for laser power of 400 W. Hence, it can be concluded that increasing the laser power has had more significant impact on the AISI 304/1060 joint elongation rate. Additionally, it should be noted that the brittle fracture behavior of AISI 420/1060 decreased the joint elongation rate of the joint, although the ultimate tensile strength of the joint is slightly higher than AISI 304/1060 joint because of having different materials properties.

Totally, the AISI 304/1060 depicted more ductile fracture mechanism with higher elongation rate according to creation of dissimilar fusion zone. The majority of samples either AISI 304 or AISI 420 failure from heat affected area or fusion line of the AISI 1060 steel. As a results, besides laser welding process parameters, the dissimilar melt pool microstructure, melt pool dimension and failure mechanism are the factors have impact on the joint tensile stress and elongation rate.

The effect of focal length on the tensile stress and strain rate of AISI 420/1060 joint for experimental condition Nos. 1, 3 and 14 was presented in Fig. 29 to clearly investigate the stress variation according to the strain rate of the joint. It is clearly observed that in case the laser power of 350 W and welding speed of 250 mm/min were utilized, increasing the focal distance from −2 to 6 mm related to the welded sample surface, clearly decreased the tensile stress about 18 percent. Additionally, the strain rate reduced about 5 percent and the general trend of stress/strain curve implies that a brittle fracture has been the predominant failure mode for AISI 420/1060 joint. By increasing the focal distance, a notable reduction in energy density from 3.96 to 2.22 W/cm^2 (about 40 %) induced the reduction of stress rate about 18 percent due to decreasing the melt pool volume.

Fig. 30 depicts the effect of increasing the focal distance on the tensile stress and strain rate of the AISI 304/1060 joint. Augmentation the focal point position related to the workpiece surface from −2 to 6 mm significantly altered both the joint strain rate and tensile stress of the welded joint. In case the laser beam focal position located the distance of (−2 mm) below the workpiece surface, the highest values for both stress and strain rates were gained. Although the value of the tensile stress for AISI 304/1060 joint is considerably lower than AISI 420/1060 joint, the strain rate of AISI 304/1060 joint at focal distance of −2 mm is remarkably higher about 17 percent compared to the 5 percent for AISI 420/1060 joint. By Increasing the focal distance from −2 to 6 mm notably diminished the strain rate about 12 percent. As it is clearly observed in Fig. 30, increasing the focal distance from −2 to 6 mm not only reduced the ultimate tensile stress of the joint about 33 percent, but also significantly decreased the strain rate about 70 percent which is the highest reduction rate among all investigated parameters. Hence, it can be concluded that by increasing the focal distance beyond 2 mm, the elongation rate dramatically decreased. From the graph slopes and trends, it could be inferred that the failure mode of AISI 304/1060 joint obeys the ductile fracture mode compared to the AISI 420/1060 joint.

6. Conclusion

- In this study, a clear comparison has made between two with two dissimilar joint of authentic and ferritic stainless steel with AISI 1060 steel has been performed via design of experiments to comprehensively address the laser welding process parameters effect on dissimilar weld joint characterization by considering the joints microstructure, mechanical properties, temperature field during welding and weld defects.
- The ANOVA findings suggest that the variations in temperature surrounding the 304 stainless steel melt pool is predominantly influenced by the welding linear velocity and laser beam power. Conversely, the temperature of 420 stainless steel is notably impacted by the laser beam deviating to that side.
- A significant decrease in the temperature of the surrounding melt pool region at 304 stainless steel from 240 °C to 70 °C was observed when the welding speed was increased and the beam irradiation was directed towards AISI 1060 steel. The rate of temperature reduction remained relatively constant when transferring the laser beam to 304 steel and increasing the welding speed, with only a 15 % variation.

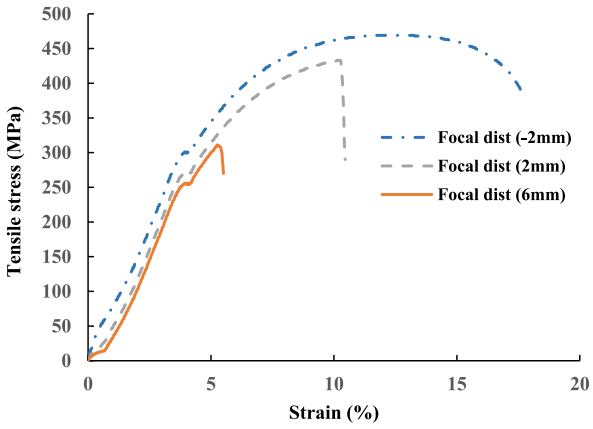

Fig. 30. Tensile stress diagram for AISI 304/1060 at laser power of 350 W, welding speed of 250 mm/min and different focal distances.

- A clear comparison between the temperature distribution with different joint configuration illustrates that distinct relation between the temperature variation rate and different thermal conductivity coefficient of AISI 1060 with different AISI 304 and 420 joint configuration resulted different temperature distribution. The numerical simulation results are in good agreement with experimental results via the temperature distribution and weld joint geometry
- The tensile strength of the joints was greatly impacted by the beam power, welding speed, and the deviation of the laser beam position. Additionally, the relationship between beam power and beam deflection had the most notable effect on the tensile strength of the welded 420 stainless steel and AISI 1060 AISI 1060 steel.
- The weld joint microstructure for 420 stainless steel –AISI 1060 steel joint at fusion boundary zone consists of columnar dendrites and skeletal columnar ferrite. At the center of fusion zone, a cellular-type structure is seen. For 304 stainless steel joint, the fusion zone has composed of a remarkable part of skeletal delta-ferrite and dendritic microstructure at austenite matrix microstructure.
- Augmenting the laser power causes a rise in tensile strength and as a result, an increase in the depth of the cavities and an increase in the energy of the fracture of the cross section caused by the ductile fracture mechanism in 304 steel and the fracture mechanism in carbon brittle steel.
- The depth of the cavities created at the AISI 1060 steel side of joint with AISI420 was clearly deeper than AISI 304 steel. The fracture surface of the material for AISI 1060 steel also indicates a brittle fracture mechanism.
- Both joint configuration depicts some steeper cavities with more dimples in case of focal point position of 0 mm. Welding at focal point position has had higher penetration rate and thereby created higher strength joints.
- Increasing the temperature gradient near AISI 1060 steel can create intense temperature gradient and reduce porosity formation near the fusion line of the AISI 1060 steel. It was evidently observed that the parameters including the power of the laser beam, speed of welding and deviating the laser beam incident position to the both base metals sides had the remarkable impact on both dissimilar joints tensile strength, respectively.

CRediT authorship contribution statement

Akbar Zarei: Writing – original draft, Data curation, Conceptualization. **Mohammad Akbari:** Validation, Supervision, Investigation. **Ali Abdollahi:** Methodology, Formal analysis. **Hamid Soleimanimehr:** Resources, Project administration.

Declaration of competing interest

The authors declare that they have no known competing financial interests or personal relationships that could have appeared to influence the work reported in this paper.

References

[1] J. Wu, E.G. Roibu, W. Hou, R. Delgado-Ruiz, G.E. Romanos, Thermal effects of 445 nm laser irradiation on the bovine tongue tissues ex vivo, Journal of Optics and Photonics Research (2024). https://doi.org/10.47852/bonviewJOPR42022543.
[2] Y. Zhang, M.H.R. Dehkordi, M.J. Kholoud, H. Azimy, Z. Li, M. Akbari, Numerical modeling of the temperature distribution and melt flow in dissimilar fiber laser welding of duplex stainless steel 2205 and low alloy steel, Opt Laser. Technol. 174 (2024) 110575.
[3] M. Azari, E. Rasti, M.H.R. Dehkordi, H. Azimy, A. Zarei, S.A. Bagherzadeh, Investigation of temperature distribution and melt pool microstructure in laser fusion welding of Inconel 625 superalloy, J. Laser Appl. 33 (2) (2021) 022015.
[4] J. Zhao, Z. Wang, Y. Han, Stability analysis of elastic steel beam-column under high temperature, International Journal of Hydromechatronics 5 (1) (2022) 44–79.
[5] L. Wang, Y. Rong, Review on processing stability, weld defects, finite element analysis, and field assisted welding of ultra-high-power laser ($\geq$ 10 kW) welding, International Journal of Hydromechatronics 5 (2) (2022) 167–190.
[6] A. Tufaile, A. P. B Tufaile, Investigating isogyres in ferrofluids and horocycles from parlaseric circle in a ferrocell, Journal of Optics and Photonics Research (2024). https://doi.org/10.47852/bonviewJOPR42022329.
[7] C. Sun, M.H.R. Dehkordi, M.J. Kholoud, H. Azimy, Z. Li, Systematic evaluation of pulsed laser parameters effect on temperature distribution in dissimilar laser welding: a numerical simulation and artificial neural network, Opt Laser. Technol. 163 (2023) 109407.
[8] J. Zhang, M.H.R. Dehkordi, M.J. Kholoud, H. Azimy, S. Daneshmand, Experimental and numerical study of melt flow, temperature behavior and heat transfer mechanisms during the dissimilar laser welding process, Opt Laser. Technol. 180 (2024) 111521.
[9] A.G. Bracamonte, Hybrid nanoplatforms and silica nano-hole particles intended for enhanced energy modes: light-scattering studies toward lasers developments, Journal of Optics and Photonics Research (2024). https://doi.org/10.47852/bonviewJOPR42022233.
[10] J. Li, T. Sui, X. Dong, F. Gu, N. Su, J. Liu, C. Xu, Large eddy simulation studies of two-phase flow characteristics in the abrasive flow machining of complex flow ways with a cross-section of cycloidal lobes, International Journal of Hydromechatronics 5 (2) (2022) 136–166.
[11] A. Mosavi, A. Soleimani, A. Karimi, M. Akbari, A. Karimipour, A. Karimipour, Investigating the effect of process parameters on the mechanical properties and temperature distribution in fiber laser welding of AISI304 and AISI 420 sheet using response surface methodology, Infrared Phys. Technol. 111 (2020) 103478.
[12] J.R. Berretta, W. de Rossi, M.D.M. das Neves, I.A. de Almeida, N.D.V. Junior, Pulsed Nd: YAG laser welding of AISI 304 to AISI 420 stainless steels, Opt Laser. Eng. 45 (9) (2007) 960–966.
[13] M. Handbook, Welding, Brazing, and Soldering, vol. 6, 1993, p. 322 *(No Title)*.
[14] A. Karimi, A. Karimipour, M. Akbari, M.M. Razzaghi, M.J. Ghahderijani, Investigating the mechanical properties and fusion zone microstructure of dissimilar laser weld joint of duplex 2205 stainless steel and A516 carbon steel, Opt Laser. Technol. 158 (2023) 108875.
[15] M.J. Rawa, M.H.R. Dehkordi, M.J. Kholoud, N.H. Abu-Hamdeh, H. Azimy, Using the numerical simulation and artificial neural network (ANN) to evaluate temperature distribution in pulsed laser welding of different alloys, Eng. Appl. Artif. Intell. 126 (2023) 107025.
[16] M. Nekouie Esfahani, J. Coupland, S. Marimuthu, Microstructural and mechanical characterisation of laser-welded high-carbon and stainless steel, Int. J. Adv. Des. Manuf. Technol. 80 (2015) 1449–1456.
[17] M.N. Esfahani, J. Coupland, S. Marimuthu, Microstructure and mechanical properties of a laser welded low carbon–stainless steel joint, J. Mater. Process. Technol. 214 (12) (2014) 2941–2948.
[18] M. Torkamany, S. Tahamtan, J. Sabbaghzadeh, Dissimilar welding of carbon steel to 5754 aluminum alloy by Nd: YAG pulsed laser, Mater. Des. 31 (1) (2010) 458–465.

[19] Z. Sun, R. Karppi, The application of electron beam welding for the joining of dissimilar metals: an overview, J. Mater. Process. Technol. 59 (3) (1996) 257–267.
[20] Z. Sun, T. Moisio, Laser beam welding of austenitic/ferritic dissimilar steel joints using nickel based filler wire, Mater. Sci. Technol. 9 (7) (1993) 603–608.
[21] C.L. Poornima, C.S. Rao, N. Varma, Numerical simulation on the laser beam welded UNS S32304 duplex steel and 304L stainless steel joints using ANSYS and response surface methodology, Int. J. Interact. Des. Manuf. (2024). https://doi.org/10.1007/s12008-024-01860-9.
[22] A.K. Unni, M. Vasudevan, Determination of heat source model for simulating full penetration laser welding of 316 LN stainless steel by computational fluid dynamics, Mater. Today: Proc. 45 (2021/01/01/, 2021) 4465–4471.
[23] Y. Ai, X. Liu, Y. Huang, L. Yu, Numerical analysis of weld bead formation process in the dissimilar material fiber laser welding, J. Laser Appl. 33 (4) (2021) 042055.
[24] C. Cui, X. Cui, X. Ren, T. Liu, J. Hu, Y. Wang, Microstructure and microhardness of fiber laser butt welded joint of stainless steel plates, Mater. Des. 49 (2013) 761–765.
[25] W. Meng, Z. Xu, Q. Ma, X. Yin, J. Fang, Pulse fiber laser welding of AISI 321-AISI 405 stainless steel thick plates butt joints, J. Mater. Process. Technol. 271 (2019) 214–225.
[26] L. Yan, J.E. Jam, M.H. Beni, M.J. Kholoud, D. Baleanu, M.E. Shahraki, F. Ghaemi, Effect of laser welding parameters on the temperature distribution, microstructure and mechanical properties of dissimilar weld joint of Inconel 625 and stainless steel 304, Int. Commun. Heat Mass Tran. 131 (2022) 105859.
[27] Y. Geng, M. Akbari, A. Karimipour, A. Karimi, A. Soleimani, M. Afrand, Effects of the laser parameters on the mechanical properties and microstructure of weld joint in dissimilar pulsed laser welding of AISI 304 and AISI 420, Infrared Phys. Technol. 103 (2019) 103081.
[28] W. Wu, S. Hu, J. Shen, Microstructure, mechanical properties and corrosion behavior of laser welded dissimilar joints between ferritic stainless steel and carbon steel, Mater. Des. 65 (2015) 855–861.
[29] M. Torkamany, J. Sabbaghzadeh, M. Hamedi, Effect of laser welding mode on the microstructure and mechanical performance of dissimilar laser spot welds between low carbon and austenitic stainless steels, Mater. Des. 34 (2012) 666–672.
[30] E. Anawa, A.-G. Olabi, Control of welding residual stress for dissimilar laser welded materials, J. Mater. Process. Technol. 204 (1–3) (2008) 22–33.
[31] E. Anawa, A.-G. Olabi, Using Taguchi method to optimize welding pool of dissimilar laser-welded components, Opt Laser. Technol. 40 (2) (2008) 379–388.
[32] A. Olabi, G. Casalino, K. Benyounis, M.S.J. Hashmi, An ANN and Taguchi algorithms integrated approach to the optimization of CO2 laser welding, Adv. Eng. Software 37 (10) (2006) 643–648.
[33] A.H. Committee, Properties and Selection: Irons, Steels, and High-Performance Alloys, ASM international, 1990.
[34] M.J. Kholoud, M. Akbari, Numerical investigation of molten pool dimension, temperature field and melting flow during pulsed laser welding of Ti-6Al-4V alloy sheets with different thicknesses, J. Laser Appl. 33 (3) (2021) 032012.
[35] Y. Ai, P. Jiang, C. Wang, G. Mi, S. Geng, Experimental and numerical analysis of molten pool and keyhole profile during high-power deep-penetration laser welding, Int. J. Heat Mass Tran. 126 (2018/11/01/, 2018) 779–789.
[36] P. Xia, F. Yan, F. Kong, C. Wang, J. Liu, X. Hu, S. Pang, Prediction of weld shape for fiber laser keyhole welding based on finite element analysis, Int. J. Adv. Des. Manuf. Technol. 75 (1) (2014/10/01, 2014) 363–372.
[37] Y. Ai, P. Jiang, X. Shao, P. Li, C. Wang, A three-dimensional numerical simulation model for weld characteristics analysis in fiber laser keyhole welding, Int. J. Heat Mass Tran. 108 (2017/05/01/, 2017) 614–626.
[38] B. Chang, C. Allen, J. Blackburn, P. Hilton, D. Du, Fluid flow characteristics and porosity behavior in full penetration laser welding of a titanium alloy, Metall. Mater. Trans. B 46 (2) (2015/04/01, 2015) 906–918.
[39] J.G. Berryman, S.C. Blair, Kozeny–Carman relations and image processing methods for estimating Darcy's constant, J. Appl. Phys. 62 (6) (1987) 2221–2228.
[40] B. Hu, S. Hu, J. Shen, Y. Li, Modeling of keyhole dynamics and analysis of energy absorption efficiency based on Fresnel law during deep-penetration laser spot welding, Comput. Mater. Sci. 97 (2015/02/01/, 2015) 48–54.
[41] A.K. Maurya, C. Pandey, R. Chhibber, Dissimilar welding of duplex stainless steel with Ni alloys: a review, Int. J. Pres. Ves. Pip. 192 (2021/08/01/, 2021) 104439.